DESIGN OF PARAMETRICALLY FORCED PATTERNS AND QUASIPATTERNS

A.M. RUCKLIDGE* AND M. SILBER†

Abstract. The Faraday wave experiment is a classic example of a system driven by parametric forcing, and it produces a wide range of complex patterns, including superlattice patterns and quasipatterns. Nonlinear three-wave interactions between driven and weakly damped modes play a key role in determining which patterns are favoured. We use this idea to design single and multi-frequency forcing functions that produce examples of superlattice patterns and quasipatterns in a new model PDE with parametric forcing. We make quantitative comparisons between the predicted patterns and the solutions of the PDE. Unexpectedly, the agreement is good only for parameter values very close to onset. The reason that the range of validity is limited is that the theory requires strong damping of all modes apart from the driven pattern-forming modes. This is in conflict with the requirement for weak damping if three-wave coupling is to influence pattern selection effectively. We distinguish the two different ways that three-wave interactions can be used to stabilise quasipatterns, and present examples of 12-, 14- and 20-fold approximate quasipatterns. We identify which computational domains provide the most accurate approximations to 12-fold quasipatterns, and systematically investigate the Fourier spectra of the most accurate approximations.

Key words. Pattern formation, quasipatterns, superlattice patterns, mode interactions, Faraday waves.

AMS subject classifications. 35B32, 37G40, 52C23, 70K28, 76B15

1. Introduction. The classic Faraday wave experiment consists of a horizontal layer of fluid that spontaneously develops a pattern of standing waves on its surface as it is driven by vertical oscillation with amplitude exceeding a critical value; see [2, 33, 44] for recent reviews and surveys. Many other experimental, biological and environmental systems also form patterns [14,31], but Faraday wave experiments have consistently produced patterns with remarkably high degrees of symmetry. One consequence of this is that, over the years, Faraday wave experiments have repeatedly produced new patterns of behaviour that went beyond the existing range of theoretical understanding and required the development of new ideas for their explanation. For example, in the early 1990's, *quasipatterns* were discovered in two different Faraday wave experiments, one with a low-viscosity deep layer of fluid with single-frequency forcing [5–7], and the other with a high-viscosity shallow layer of fluid and forcing with two commensurate temporal frequencies [20]. These patterns are periodic in time but are quasiperiodic in any spatial direction, that is, the amplitude of the pattern (taken along any direction in the plane) can be regarded as the sum of waves with incommensurate spatial frequencies. In spite of this, the spatial Fourier transforms of quasipatterns have 8, 10 or 12-fold rotational order. Quasipatterns are of course

*Department of Applied Mathematics, University of Leeds, Leeds LS2 9JT, UK

†Department of Engineering Sciences and Applied Mathematics, and Northwestern Institute on Complex Systems, Northwestern University, Evanston, IL 60208, USA

related to quasicrystals [54], and quasipatterns have been found in nonlinear optical systems [30], in shaken convection [51, 65] and in liquid crystals [37] as well as the Faraday wave experiment [2, 5–7, 20, 34]. There is, as yet, no satisfactory theoretical understanding of the formation of quasipatterns owing to the problem of small divisors [52].

Theoretical efforts aimed at understanding the pattern selection problem have centered around *weakly nonlinear theory*. The calculations for the real Faraday wave problem, with finite depth and non-zero viscosity, are difficult (these involve solving the Navier–Stokes equations with a free surface boundary condition [58]). Most calculations aimed at producing superlattice patterns and quasipatterns have focussed on simpler equations, such as the Zhang–Viñals [68] equations, which model Navier–Stokes when the depth is infinite and the viscosity is small, or on model equations, such as variations on the Swift–Hohenberg equation [23, 38, 43] or the Fitzhugh–Nagumo equations [16].

Nonlinear three-wave resonant interactions have long been recognised as playing a key role in pattern selection in Faraday wave experiments, or other situations where complex patterns are found [20, 42, 46, 69]. A series of papers [48–50, 56, 57, 62, 63] has developed this idea, using symmetry considerations to understand pattern selection in Faraday wave experiments with two-frequency forcing, exploiting the three-wave resonant interactions in the context of weakly broken Hamiltonian structure. This approach was able to explain several of the experimentally observed superlattice patterns, and suggested ways of designing multi-frequency forcing functions that could be used to control which patterns would emerge [49, 62, 63]. The approach is in principle predictive, but has only been used to determine which additional frequencies to add to the forcing function in order to make observed patterns more robust [2, 17, 21]. The theory has not been tested quantitatively against solutions of a pattern-forming system, though weakly nonlinear coefficients have been computed for the Zhang–Viñals equations [50, 62] and, more recently, for the Navier–Stokes equations in the infinite depth case [58].

The main goal of this paper is to come to a greater understanding of some of the complex patterns that are found in high-precision large aspect ratio Faraday wave experiments. Much of the complexity arises from using two or more frequencies in the forcing of the experiment, and recent work [50, 62] explains in principle how to connect the amplitudes and phases of the various components of the forcing frequencies to the nonlinear pattern selection problem. The existing theory provides rules of thumb for designing forcing functions that should encourage the appearance of particular patterns, and it seems to work well, at least qualitatively, and at least in some circumstances [2, 17, 21].

We take the point of view that in order to claim convincingly that we understand the pattern selection process in these problems with multi-frequency forcing, we should be able to predict *in advance* which patterns will be found for different parameter

values, we should be able to predict the amplitudes and range of stability of the patterns, and we should test against a pattern forming system that is not constrained to produce only a limited range of patterns. In order to have a flexible framework for testing predictions, we have devised a partial differential equation (PDE) with multi-frequency forcing (3.1) that shares many of the characteristics of the real Faraday wave experiment, but that has easily controllable dissipation and dispersion relations, and simple nonlinear terms. The linear behaviour of the PDE reduces to the damped Mathieu equation, with subharmonic and harmonic tongues, and the simple quadratic and cubic nonlinearities allow three-wave interactions. The PDE has a Hamiltonian limit, but it differs from the real situation in the details of its dispersion relation, and the lack of any coupling to a large-scale mean flow. Notwithstanding these differences, the PDE allows us to explore in detail some of the generic issues surrounding pattern selection in very large aspect pattern forming systems with parametric forcing. A preliminary discussion of the question of quasipattern selection in the new model PDE can be found in [53].

In section 2, we review the details of how resonant three-wave interactions influence pattern selection. The main idea is that two pattern-forming modes, with wavevectors separated by an angle θ, are coupled to a weakly damped mode, and this coupling can lead to the angle θ either featuring in the resulting pattern or being eliminated from the resulting pattern [20, 42, 46, 69]. We introduce the model PDE in section 3, and describe its linear and nonlinear features in sections 4 and 5. Appendix A gives full details of the weakly nonlinear calculations.

In section 6 we devise a forcing function that stabilises the 22° superlattice patterns that have been observed in large aspect ratio Faraday wave experiments [2, 21, 34]. We compute fully nonlinear solutions of the PDE and compare the computed pattern amplitudes with those predicted by weakly nonlinear theory. This demonstrates that the agreement is quantitatively accurate only very close to onset (within 0.1%). We show that the limit on the range of validity is because of the presence of the weakly damped modes that are required for the superlattice pattern to be stabilised. Thus parameter regimes that are likely to produce the most interesting patterns, arising from coupling to weakly damped modes, are also parameter regimes where weakly nonlinear theory has the most restricted validity.

Two mechanisms have been proposed for quasipattern formation, both building on ideas of Newell and Pomeau [46], and one aim of this paper is to demonstrate that both proposed mechanisms for quasipattern formation are viable (preliminary work is reported in [53]). One mechanism applies to single frequency forced Faraday waves [68] and has been tested experimentally [67]. Another was developed to explain the origin of the two length scales in superlattice patterns [50, 63] found in two-frequency experiments [34]. The ideas have not been tested quantitatively, but have been used qualitatively to control quasipattern [2, 17] and superlattice pattern [21] formation in two and three-frequency experiments. We explore the two mechanisms

of quasipattern formation in the model PDE in sections 7 and 8.

Also in section 7, we address the distinction between true and approximate quasipatterns, as found in numerical experiments with periodic boundary conditions. Owing to the problem of small divisors, there is as yet no satisfactory mathematical treatment of quasipatterns [52]. In spite of this, the weakly nonlinear stability calculations, which are in the framework of a 12-mode amplitude expansion truncated at cubic order, prove to be a reliable guide to finding parameter values where approximate quasipatterns are stable. The fact that stable 12-fold quasipatterns are found where they are expected demonstrates that this approach provides useful information, in spite of the reservations expressed in [52]. We explore the effect of domain size on the accuracy of the approximation to a true quasipattern, and show how certain domains yield particularly accurate approximations.

In section 8, we present examples of *turbulent crystals* [46]: situations in which Fourier modes oriented more than about 30° apart do not affect each other, at the level of a cubic truncation. In this context, we find examples of 12-, 14- and 20-fold quasipatterns. These are the first examples of quasipatterns of order greater than 12 found as stable solutions of a PDE (a preliminary presentation of the 14-fold example is in [53]).

We summarise our result in section 9.

2. Theoretical background. Resonant triads have played a key role in the understanding of pattern formation [20, 42, 46, 69]. This section reviews, somewhat heuristically, the basic selection mechanisms in the case of wave patterns that are parametrically pumped by a two (or more) frequency forcing function. The details behind this summary can be found in [49, 62]. We write the forcing function as

$$f(t) = f_m \cos(mt + \phi_m) + f_n \cos(nt + \phi_n) + ..., \tag{2.1}$$

where m and n are integers, f_m and f_n are real amplitudes, and ϕ_m and ϕ_n are phases. (We could, of course, set $\phi_m = 0$ without loss of generality.) Here we consider m to be the dominant driving frequency, and focus on a pair of waves, each with wavenumber k_m and frequency $\Omega(k_m)$ specified by the dispersion relation associated with the linearised problem. These waves naturally oscillate at a frequency that is *subharmonic* to the dominant driving frequency m, so $\Omega(k_m) = m/2$ (subharmonic waves are typically the easiest to excite parametrically). The two waves have wavevectors $\boldsymbol{k}_m^{(1)}$ and $\boldsymbol{k}_m^{(2)}$, where we use the subscript to denote the frequency that excites the waves, and the superscript to index the wavevectors. We write the critical modes in the form $z_1 e^{i\boldsymbol{k}_m^{(1)}\cdot\boldsymbol{x}+imt/2}$ and $z_2 e^{i\boldsymbol{k}_m^{(2)}\cdot\boldsymbol{x}+imt/2}$ (together with their complex conjugates), neglecting the additional temporal frequency contributions to the waves. These waves will interact nonlinearly with waves $we^{i\boldsymbol{k}^{(3)}\cdot\boldsymbol{x}+i\Omega(k^{(3)})t}$, where w is a complex amplitude, $\boldsymbol{k}^{(3)} = \boldsymbol{k}_m^{(1)} + \boldsymbol{k}_m^{(2)}$ and $\Omega(k^{(3)})$ is the frequency associated with $k^{(3)}$, provided that either (1) the same resonance condition is met with the temporal frequencies, *i.e.*, $\Omega(k^{(3)}) = \frac{m}{2} + \frac{m}{2}$, as in figure 2.1(a,b), or (2) any mismatch

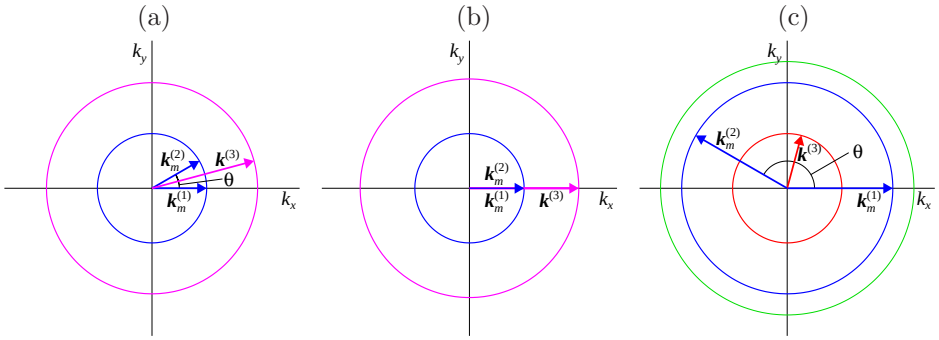

FIG. 2.1. *(a)* $1:2$ *resonance occurs between two modes with wavevectors* $\boldsymbol{k}_m^{(1)}$ *and* $\boldsymbol{k}_m^{(2)}$ *(blue), with the same wavenumber* k_m *and separated by an angle* θ*, and a third mode with wavevector* $\boldsymbol{k}^{(3)}$ *(magenta), provided* $\boldsymbol{k}^{(3)} = \boldsymbol{k}_m^{(1)} + \boldsymbol{k}_m^{(2)}$ *and* $\Omega(k^{(3)}) = 2\Omega(k_m)$*. (b) A special case of* $1:2$ *resonance in space and time occurs for* $\theta = 0$ *when the dispersion relation satisfies* $\Omega(2k_m) = 2\Omega(k_m)$*. (c) With two-frequency* $m:n$ *forcing, the nonlinear combination of two modes with wavevectors* $\boldsymbol{k}_m^{(1)}$ *and* $\boldsymbol{k}_m^{(2)}$*, and with* $\Omega(k_m) = m/2$ *(blue), can, in the presence of a second component of the forcing at frequency* n*, interact with a mode with wavevector* $\boldsymbol{k}^{(3)}$ *(red), provided* $\boldsymbol{k}^{(3)} = \boldsymbol{k}_m^{(1)} + \boldsymbol{k}_m^{(2)}$ *and* $\Omega(k^{(3)}) = |m-n|$*. Waves driven by frequency* n *(green) do not enter the resonance condition.*

$\Delta = |\Omega(k^{(3)}) - \frac{m}{2} - \frac{m}{2}|$ in this temporal resonance condition can be compensated for by the forcing function $f(t)$ (figure 2.1c). Case (1) corresponds to $1:2$ resonance, which occurs even for single frequency forcing ($f_n = 0$), and case (2) applies, for example, to two-frequency forcing with the third wave oscillating at the difference frequency: $\Omega(k^{(3)}) = |m-n|$ and $\Delta = n$. Other cases analogous to (2), such as $\Omega(k^{(3)}) = m+n$, are discussed in [62], where the special significance of the difference frequency case is explained. Note that in both cases (1) and (2), the temporal frequency $\Omega(k^{(3)})$ determines the angle θ between the wave-vectors $\boldsymbol{k}_m^{(1)}$ and $\boldsymbol{k}_m^{(2)}$ via the dispersion relation, and therefore provides a possible selection mechanism for certain preferred angles appearing in the power spectrum associated with the wavepatterns. Selecting an angle of $0°$, with $1:2$ resonance in space and time (figure 2.1b), is a special case.

The nonlinear interactions of the modes can be understood by considering resonant triad equations describing small amplitude waves, which take the form

$$\begin{aligned}
\dot{z}_1 &= \lambda z_1 + q_1 \bar{z}_2 w + (a|z_1|^2 + b|z_2|^2) z_1 + \cdots \\
\dot{z}_2 &= \lambda z_2 + q_1 \bar{z}_1 w + (a|z_2|^2 + b|z_1|^2) z_2 + \cdots \\
\dot{w} &= \nu w + q_3 z_1 z_2 + \cdots ,
\end{aligned} \tag{2.2}$$

where all coefficients are real, and the dot refers to timescales long compared to the forcing period. Here the quadratic coupling coefficients q_j are $\mathrm{O}(1)$ in the forcing in the $1:2$ resonance case, and $\mathrm{O}(|f_n|)$ in the difference frequency case [50]. For other angles θ between the wavevectors $\boldsymbol{k}_m^{(1)}$ and $\boldsymbol{k}_m^{(2)}$ we expect $q_1 \approx q_3 \approx 0$ because the temporal resonance condition for the triad of waves is not met.

Since the m frequency is dominant, the z_1 and z_2 modes will be excited (λ in-

creases through zero) while the w mode is damped ($\nu < 0$). In this case, w can be eliminated from (2.2) via center manifold reduction [27] near the bifurcation point ($w \approx \frac{q_3 z_1 z_2}{|\nu|}$), resulting in the bifurcation problem

$$\begin{aligned}\dot{z}_1 &= \lambda z_1 + (a|z_1|^2 + \tilde{b}|z_2|^2)z_1 \\ \dot{z}_2 &= \lambda z_2 + (a|z_2|^2 + \tilde{b}|z_1|^2)z_2 \ . \end{aligned} \tag{2.3}$$

These equations describe the competition between standing waves separated by an angle θ, where $\tilde{b} \equiv b + \frac{q_1 q_3}{|\nu|}$ explicitly includes the contribution from the slaved mode w, and hence depends on the angle between the two wavevectors $\boldsymbol{k}_m^{(1)}$ and $\boldsymbol{k}_m^{(2)}$.

The contribution of the damped w mode is significant whenever $q_1 q_3$ is non-negligible and the damping $|\nu|$ is not too great, and can be made more important by increasing $q_1 q_3$ and/or by decreasing the damping $|\nu|$. For instance, in the $1:2$ resonance case, for which $q_1 q_3$ is O(1), the damping can be decreased by taking $n = 2m$ in (2.1), since the w mode, with frequency m, will then be driven subharmonically by the n component of the forcing (as well as harmonically by the m component).

In the difference frequency case, the quadratic interactions rely on the presence of the n component of the forcing to allow the temporal resonance condition to be met, so $q_1 q_3$ is O($|f_n|^2$). Thus the contribution of the damped w mode to $\tilde{b}$ can be made more important in two ways: first, by increasing f_n, or second, by parametrically driving the damped mode so that $|\nu|$ is decreased. This requires a third driving frequency $p = 2|n - m|$ to be added to the forcing (2.1). In both of these instances, the relative phases of the components of the forcing matter, since the modes are being generated nonlinearly with a preferred phase. These ideas are developed systematically in [50, 62], where it is also shown that if there is an underlying Hamiltonian structure, then $q_1 q_3 < 0$ for the $1:2$ resonance, and $q_1 q_3 > 0$ in the difference frequency case provided $n > m$. Note that when $q_1 q_3 > 0$ ($q_1 q_3 < 0$) then the $\boldsymbol{k}^{(3)}$-mode makes a positive (negative) contribution to the growth rate of the mode z_2 when z_1 is present.

In order to determine more precisely whether the resonant contribution to $\tilde{b}$ is significant enough to lead to a qualitative change in the resulting pattern, it is useful to rescale the amplitudes z_1 and z_2 in (2.3) by a factor of $1/\sqrt{|a|}$. Then we obtain, for $a < 0$, the rescaled equations

$$\begin{aligned}\dot{z}_1 &= \lambda z_1 - (|z_1|^2 + B_\theta |z_2|^2)z_1 \\ \dot{z}_2 &= \lambda z_2 - (|z_2|^2 + B_\theta |z_1|^2)z_2 \ , \end{aligned} \tag{2.4}$$

where $B_\theta \equiv \frac{\tilde{b}}{a}$. Here the θ subscript indicates that the cross-coupling coefficient between the $\boldsymbol{k}_m^{(1)}$ and $\boldsymbol{k}_m^{(2)}$ modes depends on the angle θ between them.

The B_θ function has important consequences for the stability of regular patterns. As a simple example, note that stripes ($|z_1| = \sqrt{\lambda}$, $z_2 = 0$) are stable if $B_\theta > 1$, while rhombs associated with a given angle θ ($|z_1| = |z_2| = \sqrt{\lambda/(1 + B_\theta)}$) are preferred if $|B_\theta| < 1$. Moreover, if $|B_\theta| < 1$ for any angle θ, then stripes will necessarily

be unstable near onset. Since, by judicious choice of forcing frequencies we have at least some ability to control both the magnitude and sign of B_θ over some range of angles θ, we have a mechanism for enhancing or suppressing certain combinations of wavevectors in the resulting weakly nonlinear patterns. Alternatively, as suggested by [68], if we choose forcing frequencies that lead to a large $1:2$ resonant contribution at $\theta = 0$ (figure 2.1b), then the coefficient a can become large compared to b, which in turn will cause the rescaled cross-coupling coefficient B_θ to be small over a broad range of angles away from $\theta = 0$. (As $\theta \to 0$, it can be shown that $B_\theta \to 2$.) These two cases are contrasted in sections 7 and 8, with preliminary work described in [53].

Before continuing, we reiterate the constraint on using this analysis to design forcing functions that will stabilise a given pattern. In eliminating the damped mode w, we performed a center manifold reduction, which is valid provided that all non-neutral modes are linearly damped with decay rates that are bounded away from zero. The domain of validity of the reduced equations depends on the extent to which w is damped near the bifurcation point. If that damping is very weak, then the reduced equations will only be quantitatively predictive in a correspondingly small neighborhood of the bifurcation point. We point this out since, from the discussion above, it is clear that the two ways of influencing the magnitude of $\tilde{b}$, namely increasing the driving force f_n to control $q_1 q_3$, or driving the difference frequency to reduce the damping $|\nu|$, both can lead to situations where the center manifold reduction is no longer valid: the m and n modes could set in together, or the m and difference frequency modes could set in together. In either case, a codimension-two analysis could be performed, but this is beyond the scope of this paper. In practice, the severity of this constraint can only be seen by comparing predictions for the amplitudes and stability of patterns with solutions of the problem at hand (which we do systematically in section 6).

3. The model PDE. In order to explore these issues in detail, we have devised a phenomenological PDE for which the leading nonlinear coefficients in bifurcation problems such as (2.3), can be calculated relatively easily, and which is reasonably simple to integrate numerically. The equation is:

$$\begin{aligned}\frac{\partial U}{\partial t} &= (\mu + i\omega)U + (\alpha + i\beta)\nabla^2 U + (\gamma + i\delta)\nabla^4 U \\ &\quad + Q_1 U^2 + Q_2|U|^2 + C|U|^2 U + i\mathrm{Re}(U) f(t),\end{aligned} \tag{3.1}$$

where $f(t)$ is a real 2π-periodic function, $U(x, y, t)$ is a complex-valued function, with $(x, y) \in \mathbb{R}^2$, and $\mu < 0$, ω, α, β, γ and δ are real parameters, and $Q_1 = Q_{1r} + iQ_{1i}$, $Q_2 = Q_{2r} + iQ_{2i}$ and $C = C_r + iC_i$ are complex parameters.

The way the forcing function enters the PDE was chosen so that the linearised problem reduces to the damped Mathieu equation (in much the same way that hydrodynamic models of the Faraday instability reduce to this equation [3]). The PDE has the advantage that the dispersion relation can be controlled easily, and weakly nonlinear theory is relatively straightforward to compute. The linear terms are diagonal in

Fourier space, so the PDE is readily amenable to the Exponential Time Differencing numerical methods of [12]. In addition, the nonlinear terms are simple (they do not involve any derivatives), and so numerical solutions are relatively inexpensive.

One of the special features of parametric systems is that, even though pattern selection is a nonlinear process, the position of the linear stability curves often determines which resonant triad interactions are dominant. In turn, it is the resonant triad interactions rather than the details of the particular form of nonlinearity in the equation that drive the pattern selection process. For these reasons, the model PDE is a useful testing ground for results derived from symmetric bifurcation theory.

The model PDE is similar to the complex Ginzburg–Landau equation – but we point out that $U(x, y, t)$ is itself the pattern-forming field, and is not the amplitude of some other underlying pattern. With $\mu < 0$, all waves are damped in the absence of driving. Note also that the parametric forcing $f(t)$ is explicitly a function of time so that we are resolving dynamics on the fast time-scale set by the periodic forcing. In contrast, other authors [8–11, 29] have investigated Ginzburg–Landau equations that describe the slow, large spatial-scale evolution of the amplitude of an otherwise spatially homogeneous oscillatory mode arising through Hopf bifurcation. Instead of resolving the fast oscillations of the subharmonic response to the time dependent forcing, a constant-coefficient $\bar{U}$ term is introduced into the equation, proportional to the amplitude of the parametric forcing [11]. With multi-frequency forcing, other terms, such as $\bar{U}^2$, are also introduced [8–10, 29].

There are important qualitative differences, of course, between the model PDE and the Faraday wave experiment. One difference is the role of the $k = 0$ mode. In the PDE, this mode is damped ($\mu < 0$) and has a non-zero frequency ω; moreover the $k = 0$ mode can be nonlinearly excited. In the Faraday wave problem, owing to mass conservation, the $k = 0$ mode is neutral and cannot be excited, and this may have important consequences in the dynamics [13, 40]. (In the Zhang–Viñals model [68] this requirement is met since all nonlinear terms appear with an overall spatial derivative that prevents the excitation of the $k = 0$ mode.) Another important difference between the model PDE and the Faraday wave experiment is that the dispersion relations have a different structure: in the model PDE, the frequency is a polynomial function of the square of the wavenumber, but the dispersion relation for Faraday waves is more complicated [3, 4, 36]. Nonetheless, the marginal stability curves of the model PDE, especially with multi-frequency forcing, are similar to those that are observed in large aspect ratio Faraday wave experiments.

The theory developed in [50, 62] applies in the weakly damped, weakly forced regime, and certain of those results also require that the undamped problem have a Hamiltonian structure. This limit can be realised for our model (3.1) by setting

$\mu = \alpha = \gamma = C_r = 0$ and $Q_2 = -2\bar{Q}_1$. In this case, the Hamiltonian is:

$$H(U,\bar{U}) = \iint_R \left[\omega|U|^2 - \beta|\nabla U|^2 + \delta|\nabla^2 U|^2 + f(t)(\mathrm{Re}(U))^2 \right. \\ \left. - iQ_1U^2\bar{U} + i\bar{Q}_1\bar{U}^2U + \frac{C_i}{2}|U|^4\right] dxdy, \qquad (3.2)$$

and U evolves according to

$$\frac{\partial U}{\partial t} = i\frac{\delta H}{\delta \bar{U}} \ . \qquad (3.3)$$

The region R corresponds to the domain of integration of the PDE (3.1), where we have assumed periodic boundary conditions apply on ∂R. In the examples presented below, some of the parameter choices are nearly Hamiltonian (sections 7 and 8) and some are not (section 6).

4. Linear theory. The linear problem associated with (3.1) takes the form of a damped Mathieu equation for each Fourier mode $e^{i\boldsymbol{k}\cdot\boldsymbol{x}}$. Specifically, if we set $U(\boldsymbol{x},t) = e^{i\boldsymbol{k}\cdot\boldsymbol{x}}(p(t)+iq(t))$ in (3.1) linearised about $U=0$, then we obtain

$$\ddot{p} + \hat{\gamma}\dot{p} + \left(\Omega^2 + \hat{\Omega}f(t)\right)p = 0 \ , \qquad (4.1)$$

where

$$\hat{\gamma} = 2\left(-\mu + \alpha k^2 - \gamma k^4\right), \qquad \hat{\Omega} = \omega - \beta k^2 + \delta k^4, \qquad \Omega^2 = \frac{\hat{\gamma}^2}{4} + \hat{\Omega}^2 \ . \qquad (4.2)$$

We use the method of [4] to solve this linear problem for multi-frequency forcing $f(t)$, which determines the critical forcing amplitude. Further details can be found in Appendix A.

We require that the damping $\hat{\gamma}$ be positive for all k, so $\mu < 0$, $\gamma \leq 0$ and $\alpha > -\sqrt{4\gamma\mu}$. However, we do not necessarily insist that it be monotonic, which would require $\alpha \geq 0$. Non-monotonic damping is possible in the Faraday wave experiment in shallow layers: if the viscous boundary layers extend from top to bottom of the experimental container, modes with long wavelengths can be more heavily damped than short-wave modes, and indeed the first harmonic mode can be unstable at lower forcing than the subharmonic mode [35, 45]. We use non-monotonic damping for the example in section 7. Likewise, we restrict ourselves to the parameter regime where the dispersion relation $\hat{\Omega}(k)$ is non-negative and an increasing function of k^2; thus we assume $\omega \geq 0$, $\delta \geq 0$ and $\beta \leq 0$.

We will use both $1:2$ and difference frequency resonances to control how modes interact, so it is important to understand that these resonances impose further constraints on the parameters in the dispersion relation. In the case of single frequency ($m=1$) forcing $f(t) = a\cos(t+\phi)$, we expect a subharmonic instability to set in first with increasing a at a critical wavenumber k_1, which can be estimated by solving the equation $\hat{\Omega}(k_1) = \frac{1}{2}$. This estimate of k_1 is good provided the damping is not too large, and that the damping is a (nearly) monotonic function of k. The wavenumber

associated with the first harmonic instability is determined by solving $\hat{\Omega}(k_2) = 1$. These calculations, together with simple trigonometry, determine that the angle θ associated with a $1:2$ resonant triad satisfies the equation $k_2 = 2k_1 \cos\left(\frac{\theta}{2}\right)$, which has a solution provided $k_2 \le 2k_1$. Choosing a scaling of $\boldsymbol{x}$ so that $k_1 = 1$, then we find that ω, β and δ are related to θ by

$$\begin{aligned} \hat{\Omega}(k = k_1 = 1) &= \omega - \beta + \delta = \frac{1}{2} \\ \hat{\Omega}\left(k = k_2 = 2\cos\left(\frac{\theta}{2}\right)\right) &= \omega - 4\beta\cos^2\left(\frac{\theta}{2}\right) + 16\delta\cos^4\left(\frac{\theta}{2}\right) = 1 \ . \end{aligned} \tag{4.3}$$

In particular, the $1:2$ resonance will be at $\theta = 0^\circ$ ($k_2 = 2$) if we choose

$$\omega = \frac{1}{3} + 4\delta \ , \qquad \beta = -\frac{1}{6} + 5\delta \ , \tag{4.4}$$

where $\delta \in [0, \frac{1}{30}]$ ensures $\beta \le 0$ and hence a monotonic dispersion relation. The $1:2$ resonance moves to $\theta = 90^\circ$ ($k_2 = \sqrt{2}$) if we choose

$$\omega = 2\delta \ , \qquad \beta = -\frac{1}{2} + 3\delta \ , \tag{4.5}$$

where we require $\delta \in [0, \frac{1}{6}]$.

Next we consider the case of two-frequency forcing

$$f(t) = F\left(a_m \cos(mt + \phi_m) + a_n \cos(nt + \phi_n)\right) \ , \tag{4.6}$$

where m and n are coprime integers, (a_m, a_n) are relative amplitudes scaled by an overall amplitude F, and (ϕ_m, ϕ_n) are phases. We focus on a resonant triad involving two critical modes with dominant frequency $\frac{m}{2}$ and a damped difference frequency mode with dominant frequency $n - m$. We will typically take m even and n odd with $n > m$ and $n - m < \frac{m}{2}$ (*i.e.*, $\frac{n}{m} \in (1, \frac{3}{2})$). These conditions imply that the initial instability is expected to be harmonic, that the difference frequency mode decreases B_θ at the resonance angle in the Hamiltonian limit, and that the difference frequency mode has a wavenumber ($k_{\rm diff}$) that is smaller than the critical wavenumber and hence it is not too strongly damped (at least in the case of monotonic dissipation) [50]. We estimate the critical wavenumber of instability as $k \approx k_m$, where $\hat{\Omega}(k_m) = \frac{m}{2}$ and we assume a scaling such that $k_m = 1$. We then have that k_m and $k_{\rm diff}$ satisfy

$$\begin{aligned} \hat{\Omega}(k = k_m = 1) &= \omega - \beta + \delta = \frac{m}{2} \\ \hat{\Omega}(k = k_{\rm diff}) &= \omega - \beta k_{\rm diff}^2 + \delta k_{\rm diff}^4 = n - m \ , \end{aligned} \tag{4.7}$$

which we can solve for ω and β:

$$\omega = \frac{-k_{\rm diff}^2 \frac{m}{2} + (n-m)}{1 - k_{\rm diff}^2} + \delta k_{\rm diff}^2 \quad \text{and} \quad \beta = \frac{-\frac{m}{2} + (n-m)}{1 - k_{\rm diff}^2} + \delta(1 + k_{\rm diff}^2) \ . \tag{4.8}$$

Setting $k_{\rm diff} = 2\cos\left(\frac{\theta}{2}\right)$, we can relate an angle in the power spectrum of the pattern with the wavenumber $k_{\rm diff}$ of the damped mode associated with the resonant triad.

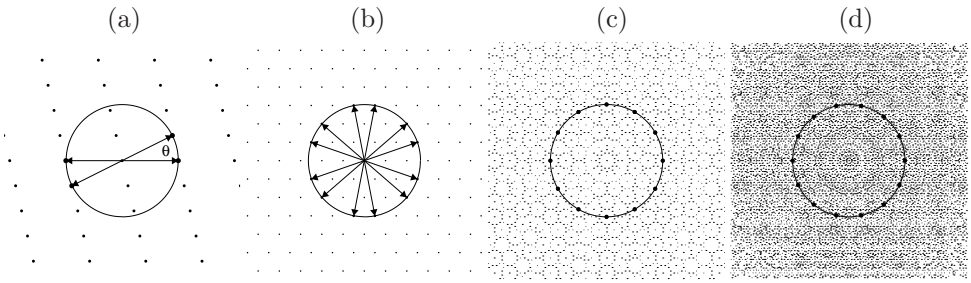

FIG. 5.1. *(a) Rhombic lattice with an angle θ between the primary wavevectors. (b) Hexagonal superlattice, with an angle of 21.8° between the most closely spaced wavevectors. (c,d) 12-fold and 14-fold quasilattices, up to 11th order and 7th order respectively [52]. See section 7 for a discussion of how these quasilattices are generated.*

For instance, for $\theta = 150^\circ$ (the complementary angle to 30°, which appears in the 12-fold quasipatterns), we have $k_{\text{diff}} = \sqrt{2-\sqrt{3}}$. Alternatively, if $\theta = 158.2^\circ$ (the complementary angle to 21.8°, which appears in the simplest hexagonal superlattice patterns), we have $k_{\text{diff}} = \frac{1}{\sqrt{7}}$.

5. Weakly nonlinear theory. Our weakly nonlinear calculations are aimed at determining the coefficients of the leading nonlinear terms in finite-dimensional bifurcation problems associated with certain families of patterns in the plane, and the corresponding lattices of wavevectors. These finite-dimensional bifurcation problems allow us to compute rigorously the relative stability of various simple planforms, *e.g.*, stripes *vs.* squares, rhombs, hexagons, and also to calculate relative stability of superlattice patterns and hexagons, stripes, and certain rhomb patterns. Moreover these calculations lead to quantitative predictions of the amplitude of the standing wave patterns as a function of the distance λ from the bifurcation point, where $\lambda \equiv (F - F_c)/F_c$ and F_c is the critical value of the overall forcing amplitude.

A simple example of such a reduction to a finite-dimensional problem was presented in Section 2, where we described the bifurcation problem associated with a pair of standing waves oriented at an angle θ relative to each other, where $\theta \in (0, \pi/2]$ was bounded away from $\pi/3$. An example rhombic lattice is shown in figure 5.1(a). In that case, the bifurcation problem consisted of a pair of amplitude equations given by (2.4), and, after appropriate scaling, there was just a single nonlinear coefficient B_θ. The details of the (numerical) computation of this coefficient from the governing PDE (3.1) are given in Appendix A. In subsequent sections of this paper we present plots of B_θ as a function of θ for certain parameter sets and forcing functions $f(t)$ used in our numerical simulations of the model PDE.

As an additional, specific example we consider patterns associated with the hexagonal superlattice that has been observed in several Faraday wave experiments [2, 21, 34]. Equivariant bifurcation theory [24] was used to derive the form of bifurcation problem [18]. This bifurcation problem describes the long-time evolution of the twelve

modes on the critical circle that are associated with patterns that tile a plane in hexagonal fashion. The critical Fourier modes associated with the 21.8° superlattice pattern are indicated in Figure 5.1(b). We label these modes as follows: (z_1, z_3, z_5) are complex amplitudes associated with wavevectors separated by 120° and, together with their complex conjugates, they comprise the modes associated with one hexagon, while (z_2, z_4, z_6) and their complex conjugates are associated with a second hexagon, rotated by approximately 21.8° relative to the first.

The form of the bifurcation problem associated with this hexagonal superlattice, to cubic order in the amplitudes, is:

$$\frac{dz_1}{dt} = \lambda z_1 + Q\bar{z}_3\bar{z}_5 - \left(|z_1|^2 + B_{60}\left(|z_3|^2 + |z_5|^2\right) + B_{22}|z_4|^2 + B_{38}|z_6|^2 + B_{82}|z_2|^2\right) z_1$$
$$\frac{dz_3}{dt} = \lambda z_3 + Q\bar{z}_5\bar{z}_1 - \left(|z_3|^2 + B_{60}\left(|z_5|^2 + |z_1|^2\right) + B_{22}|z_6|^2 + B_{38}|z_2|^2 + B_{82}|z_4|^2\right) z_3$$
$$\frac{dz_5}{dt} = \lambda z_5 + Q\bar{z}_1\bar{z}_3 - \left(|z_5|^2 + B_{60}\left(|z_1|^2 + |z_3|^2\right) + B_{22}|z_2|^2 + B_{38}|z_4|^2 + B_{82}|z_6|^2\right) z_5,$$

with similar equations for z_2, z_4 and z_6, related by symmetry. The label on the coefficients indicates the angle between pairs of modes, *e.g.*, there is an angle of approximately 82° between z_1 and z_2, while z_1 and z_4 are separated by approximately 22°. The nonlinear coefficients Q and B_{60} are computed from the governing PDEs by considering the problem of bifurcation on a simple hexagonal lattice involving a subset of the modes, while B_θ is computed for an arbitrary $\theta \neq 60°$ on a rhombic lattice. We can then read off B_{22}, B_{38} *etc.* from a graph of B_θ as required. The details are in Appendix A. Note that we have assumed that the bifurcation to a stripe planform is supercritical so that we can rescale the amplitudes to make the self–coupling coefficient $a = -1$.

The standard planforms, namely stripes, rhombs (associated with each of the angles 22°, 38°, 82°), hexagons, and superlattice patterns, correspond to equilibrium solutions of these equations. The calculation of their linear stability proceeds in a standard fashion and is summarised in [18]. In fact, owing to the presence of the quadratic term, all planforms bifurcate unstably, but because Q is typically very small for multi-frequency forcing and sufficiently weak damping [48], the planforms can be stabilised at small amplitude by secondary bifurcations. The superlattice patterns, which satisfy $|z_1| = |z_2| = \cdots = |z_6|$, come in two varieties that bifurcate together and their relative stability is unresolved at cubic order. Specifically, hexagonal superlattice patterns are associated with z_j being real, while triangular superlattice patterns are of the form $z_j = Re^{i\pi/3}$, where R is the real amplitude [55]. Which of these two superlattice patterns is favored in a given situation depends on higher order terms in the bifurcation problem. We do not calculate the coefficients of these terms and merely lump the two types of superlattice patterns together in our bifurcation diagrams.

6. Numerical experiments: selecting superlattice patterns. Motivated by experimental observations [2, 21, 34] of superlattice patterns in the Faraday wave

experiment with 6 : 7 forcing, in this section we use 6 : 7 forcing, with some additional forcing at frequency 2 to drive the difference frequency mode, in order to stabilise a 21.8° hexagonal superlattice pattern. We carry out the linear and weakly nonlinear calculations to find parameter values for which hexagonal superlattice patterns are predicted to be stable, and solve the model PDE numerically to confirm these predictions. In addition, we make quantitative comparisons between the weakly nonlinear predictions and the numerical solutions of the PDEs, comparing the predicted amplitudes and ranges of stability of the patterns. The agreement is not quantitative except at very small amplitude, and we develop an explanation for this at the end of the section.

The PDE was solved numerically using the fourth-order Runge–Kutta Exponential Time Differencing numerical method (ETD4RK) of [12]. This pseudospectral method solves the linear part exactly, excluding the parametric forcing term, which is included with the nonlinear terms. This allows the use of a timestep based on accuracy requirements, rather than numerical stability limits. Timestepping takes place in spectral space, and the timestep is chosen to be one-twentieth of the shortest of the periods of the forcing function $f(t)$, in order that the effect of the time-dependent forcing is fully resolved by the fourth-order method. The nonlinear terms are evaluated using FFTW [22]. The resolution was relatively low for the examples in this section (up to 96×56 Fourier modes), but we used up to 1536^2 Fourier modes for the largest quasipattern examples discussed below. At each timestep, the upper half of the Fourier spectrum was removed in order to dealias the cubic terms.

We choose parameters so that the mode driven subharmonically by the 6 frequency has wavenumber $k_6 = 1$: $\hat{\Omega}(k = k_6 = 1) = 3$. The wavenumber associated with 21.8° is $\frac{1}{\sqrt{7}}$, which we wish to correspond to the difference frequency $(7-6)$, so we set $\hat{\Omega}(\frac{1}{\sqrt{7}}) = 1$. This mode responds subharmonically to driving at frequency 2. Furthermore, the wavenumber associated with 81.8° is part of this superlattice pattern, and we can influence this if we set $\hat{\Omega}(\frac{4}{\sqrt{7}}) = 6$, in $1 : 2$ resonance with the primary response. This yields $\omega = \frac{2}{3}$, $\beta = -\frac{7}{3}$ and $\delta = 0$. We choose damping coefficients $\mu = -0.1$, $\alpha = 0.01$ and $\gamma = -0.15$, and nonlinear coefficients $Q_1 = 2 + i$, $Q_2 = 1 + 2i$ and $C = -1 + 30i$. Note that these parameters are not close to the Hamiltonian limit: in fact, we have chosen the nonlinear coefficients so that the $1 : 2$ interaction *reduces* the cross-coupling coefficient in the range of angles close to 90°.

The linear theory for this problem is shown in figure 6.1, confirming that modes with wavenumber close to 1 and $\frac{1}{\sqrt{7}}$ are neutral and weakly damped respectively, with $6 : 7 : 2$ forcing (figure 6.1f). For this example, we have set the phases of the two main components of the forcing equal to zero, and (after some experimentation) set the phase of the component that drives the difference mode equal to 240°.

The cross-coupling coefficient B_θ is shown in figure 6.2: with 6 forcing only, there is a dip in the curve around 90° owing to $1 : 2$ resonance at 82°. (Had we chosen parameters sufficiently close to a Hamiltonian limit, this feature would have been a

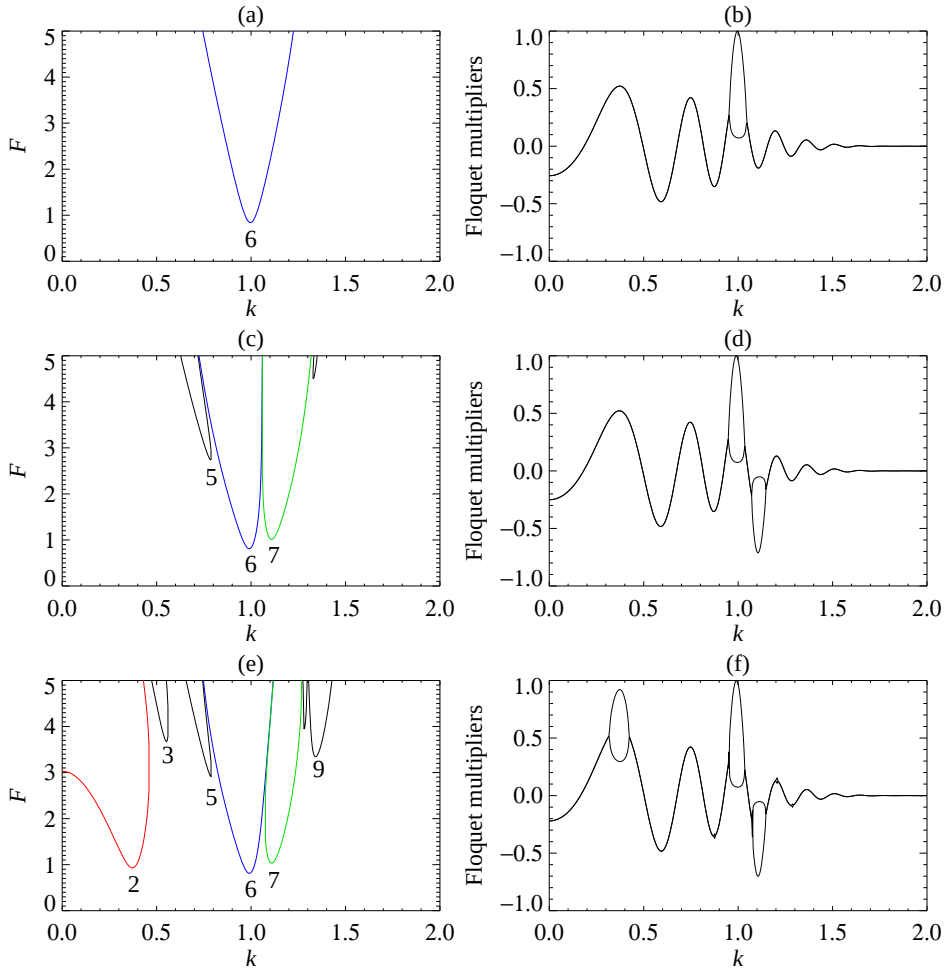

FIG. 6.1. *Linear theory for one, two and three-frequency forcing, with dispersion relation coefficients* $\omega = 2/3$, $\beta = -7/3$ *and* $\delta = 0$, *and damping coefficients* $\mu = -0.1$, $\alpha = 0.01$ *and* $\gamma = -0.1$. *(a,b)* 6 *forcing, with* $a_6 = 1$ *and* $F_c = 0.83973$. *(c,d)* $6:7$ *forcing, with* $(a_6, a_7) = (1, 1)$, $(\phi_6, \phi_7) = (0, 0)$ *and* $F_c = 0.80839$. *(e,f)* $6:7:2$ *forcing, with* $(a_6, a_7, a_2) = (1, 1, 0.45)$, $(\phi_6, \phi_7, \phi_2) = (0, 0, 240°)$, $F_c = 0.80975$ *and* $k_c = 0.9910$. *(a,c,e) show neutral stability curves, whose minima define* F_c *and the critical wavenumber (close to 1 in all cases). Curves corresponding to the response to frequency 6 are blue, to frequency 7 are green, and to twice the difference frequency are red, with the corresponding driving frequency indicated. The minimum of the red curve in (e) is close to* $k = \frac{1}{\sqrt{7}}$. *(b,d,e) show the real parts of the Floquet multipliers at the critical forcing, confirming in (b) that the instability is harmonic at* $k = 1$, *in (d) that modes corresponding to frequency* 7 *are subharmonic but damped, and in (f) that modes with wavenumber close to* $\frac{1}{\sqrt{7}}$ *are weakly damped.*

peak rather than a dip [50].) With $6:7$ forcing, the dip at 22°, corresponding to the difference frequency, is visible, even though this frequency is not forced directly. Finally, with $6:7:2$ forcing, we can control the depth of the dip at 22°. An additional feature at 43° is visible, corresponding to frequency 4, in $1:2$ resonance

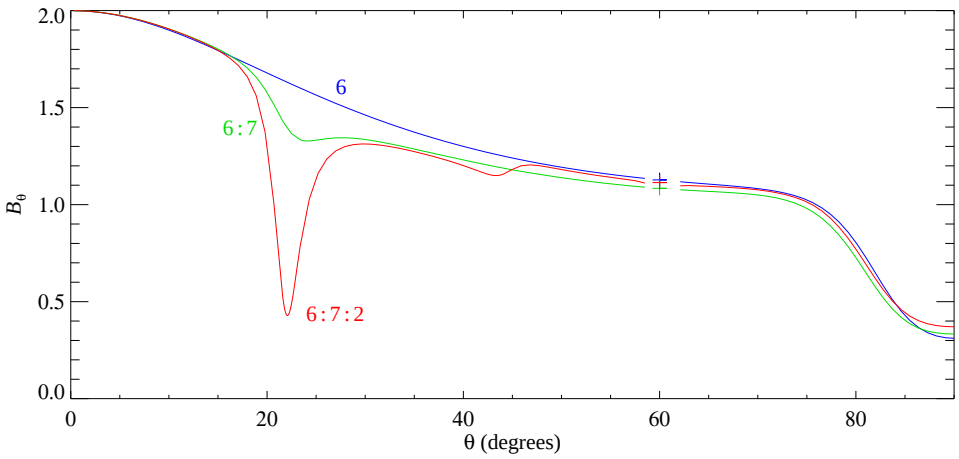

FIG. 6.2. *B_θ, with linear parameters as in figure 6.1 and nonlinear coefficients $Q_1 = 2 + i$, $Q_2 = 1 + 2i$, $C = -1 + 30i$. The blue curve is with 6 forcing only: the dip at 90° is because of 1 : 2 resonance with frequency 6. The green curve has 6 : 7 forcing: note the dip starting at 22°, corresponding to the difference frequency, even though this frequency is not forced directly. The red curve has 6 : 7 : 2 forcing: note the pronounced dip at 22°, and the smaller dip around 43°, corresponding to frequency 4 (which is in 1 : 2 resonance with frequency 2). B_{60} is calculated separately, as described in Appendix A. The relevant coefficients are $B_{22} = 0.46$, $B_{38} = 1.23$, $B_{60} = 1.11$ and $B_{82} = 0.63$.*

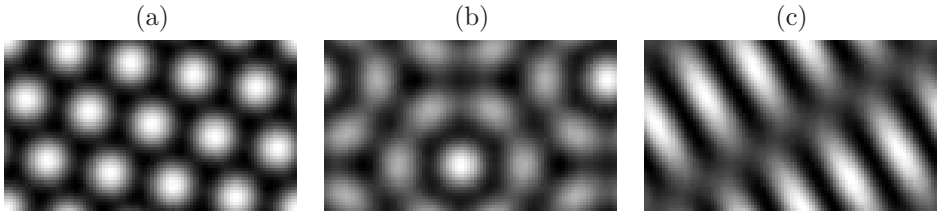

FIG. 6.3. *With 6 : 7 : 2 frequency forcing at (a,b) 1.004 and (c) 1.02 times critical, we find hexagons, a superlattice pattern, and 22° rhombss, with appropriate initial conditions. The resolution was 96×56 Fourier modes, and the domain is rectangular, $2\sqrt{7} \times 2\sqrt{7/3}$ critical wavelengths, big enough to fit two copies of the superlattice pattern. The grey-scale represents the real part of $U(x, y, t)$ with t equal to an integer multiple of 2π. The linear and nonlinear parameter values are as in figures 6.1(e,f) and 6.2.*

with frequency 2.

Solutions of the PDE with 6 : 7 : 2 forcing are shown in figure 6.3, confirming that hexagons, superhexagons and 22° rhombs are all stable solutions for different parameter values.

In figure 6.4, we make quantitative comparison between the amplitudes and stability of these patterns as numerical solutions of the PDE, and the values predicted by weakly nonlinear theory, for forcing up to 1.02 times critical. In addition, we show the results of one-dimensional simulations, which recover the unstable stripe pattern.

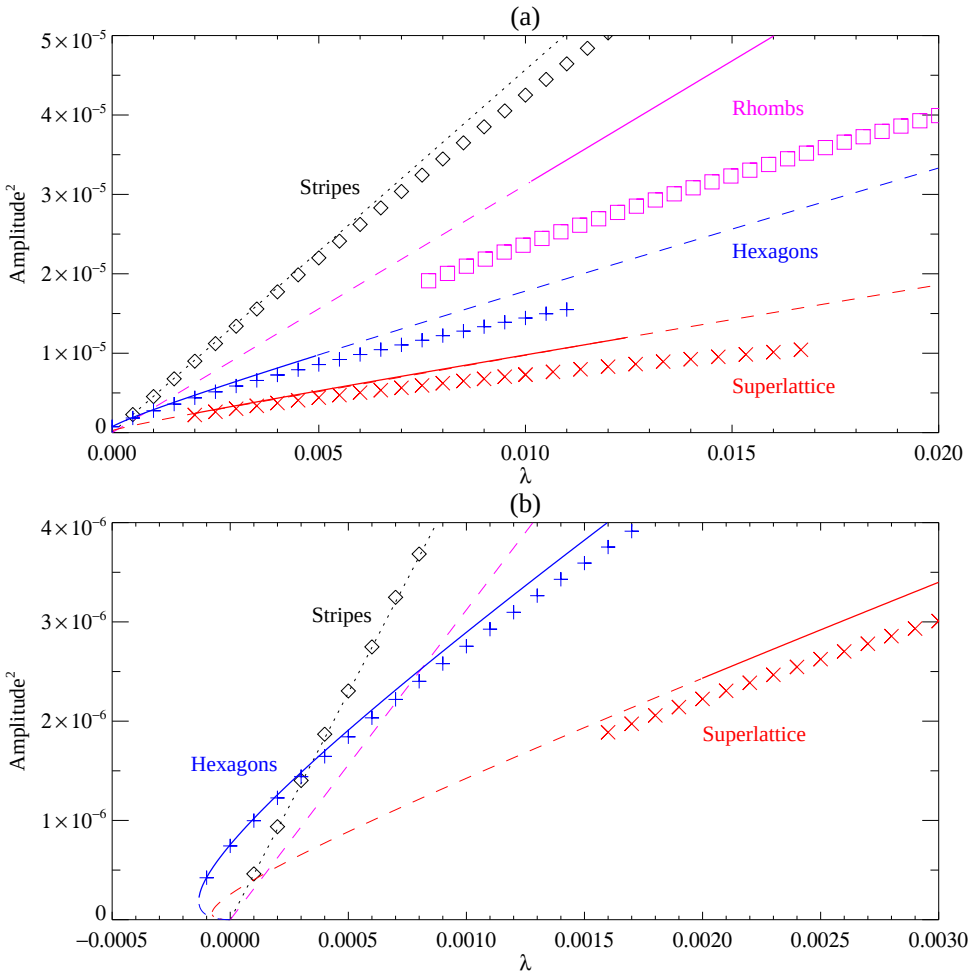

FIG. 6.4. *Amplitudes of hexagons (blue), the superlattice pattern (red), 22° rhombs (magenta) and stripes (black) as a function of λ for $6:7:2$ forcing. Using weakly nonlinear theory, we denote stable solutions with solid lines and unstable solutions with dashed and dotted lines. We also denote numerically computed stable solutions of the PDEs by $+$ for hexagons, $\times$ for the superlattice pattern, $\square$ for rhombs, and $\diamond$ for (unstable) stripes. The amplitudes of the PDE solutions are computed by matching the time evolution of the $k = 1$ modes to the linear response functions. (b) is a detail of (a), showing that the agreement between weakly nonlinear theory and the PDEs improves very close to onset.*

In all cases, numerical solutions of the PDE agree with the weakly nonlinear prediction, provided we are close enough to onset (we have confirmed this by plotting the data on a logarithmic scale). Secondary bifurcations, which delimit parameter intervals where the patterns are stable, are also recovered, although the agreement is only qualitatively correct.

It is notable that the agreement between the amplitudes predicted by weakly nonlinear theory and measured from PDE simulations is not particularly good for the

multi-mode patterns, when compared to the much better agreement in the case of stripes. The reason for this lack of quantitative agreement for the complex patterns, and for the difference between the complex patterns and stripes, can be understood by going to higher order in the center manifold reduction that was performed to go from (2.2) to (2.3). We recall the framework: there are two weakly excited modes with amplitudes z_1 and z_2, and a damped mode w, which evolve according to:

$$\begin{aligned}\dot{z}_1 &= \lambda z_1 + q_1 \bar{z}_2 w + (a|z_1|^2 + b|z_2|^2) z_1, \\ \dot{z}_2 &= \lambda z_2 + q_1 \bar{z}_1 w + (a|z_2|^2 + b|z_1|^2) z_2, \\ \dot{w} &= \nu w + q_3 z_1 z_2,\end{aligned} \tag{6.1}$$

where all coefficients are real, and $\nu < 0$. We have discarded those higher order terms that do not play a role in the centre manifold reduction in order to emphasise the effect of the higher-order nonlinear terms that appear as a result of the reduction. We express w on the centre manifold as a power series in z_1 and z_2, and perform a centre manifold reduction to find

$$w = -\frac{q_3}{\nu} z_1 z_2 + \frac{q_3(q_1 q_3 - (a+b)\nu)}{\nu^3} \left(|z_1|^2 + |z_2|^2\right) z_1 z_2 + \cdots, \tag{6.2}$$

which results in

$$\begin{aligned}\dot{z}_1 &= \lambda z_1 + (a|z_1|^2 + \tilde{b}|z_2|^2) z_1 + \frac{q_1 q_3(q_1 q_3 - (a+b)\nu)}{\nu^3} \left(|z_1|^2 + |z_2|^2\right) |z_2|^2 z_1 + \cdots, \\ \dot{z}_2 &= \lambda z_2 + (a|z_2|^2 + \tilde{b}|z_1|^2) z_2 + \frac{q_1 q_3(q_1 q_3 - (a+b)\nu)}{\nu^3} \left(|z_1|^2 + |z_2|^2\right) |z_1|^2 z_2 + \cdots,\end{aligned} \tag{6.3}$$

where $\tilde{b} = b - q_1 q_3/\nu$ as before. In order for the w mode to influence the coupling constant $B_\theta = \tilde{b}/a$, and so produce interesting patterns, the quadratic coefficients q_1 and q_3 must be non-zero (the modes must be in three-wave resonance) and ν must be small (the mode must be weakly damped). However, if ν is small, the ν^3 in the denominator of the quintic terms imply that these high-order terms will be important exactly where the most interesting patterns will be found. Indeed, the graphs of amplitude against λ in figure 6.4 are well fit by a quintic polynomial.

In contrast, the stripe pattern involves damped modes at $k = 0$ and $k = 2$, and it can be seen from figure 6.1(f) that these modes are well damped, so there is no reason for quantitative agreement not to extend to larger values of λ, and indeed it does.

One can estimate the range of validity of the cubic truncation of (6.3) when λ and ν are both small. In the case of rhombs, the linear and cubic terms balance when $|z_1|^2 = |z_2|^2 = \mathcal{O}(\lambda\nu)$. The quintic terms are thus smaller than the linear and cubic terms when $|\lambda| \ll |\nu|$, which is what one would expect: the center manifold reduction is valid when all modes that are eliminated are heavily damped compared to the modes that are retained.

Therefore, this codimension-one approach to finding interesting patterns has the smallest range of validity exactly where the patterns are most likely to be interest-

ing. A proper treatment would require consideration of the codimension-two problem $(\lambda, \nu) = (0, 0)$, which is beyond the scope of this paper.

A further complication in the Faraday wave situation (and in our model PDE) is that in order for the interaction between the primary harmonic modes (driven by the m forcing) and the weakly damped difference frequency modes $(n - m)$ to take place, the frequency n must be present in the forcing function: the quadratic coefficients q_1 and q_3 increase with the strength of the forcing f_n, so the interaction is strongest when f_n is largest. This implies that the subharmonic mode driven by frequency n is itself only weakly damped, and will be excited if f_n is increased beyond its critical value. Experimental evidence suggests that the codimension-two point (or bicritical point), where the primary harmonic (m) and subharmonic (n) modes are both neutral, is an organising centre for the dynamics [2, 20, 34]. (There has been relatively little progress on the theoretical understanding of the bicritical point, apart from a study in the case of a single frequency [66] and in a few particular cases for two-frequency excitation [48,49].) Therefore, the problem should really be treated as a codimension-three interaction between primary harmonic modes and subharmonic modes, as well as weakly damped difference frequency modes.

Notwithstanding these complications, it is clear that the idea that pattern selection is being influenced by three-wave coupling to weakly damped modes is fundamentally correct, and the codimension-one approach, while having limited quantitative agreement with PDE simulations, is clearly providing the correct qualitative interpretation of the observed patterns.

7. Numerical experiments: 12-fold quasipatterns. In the previous section, we demonstrated how to stabilise simple patterns by driving the difference frequency. In this section, we show how this mechanism can be used to predict parameter values for stable approximate 12-fold quasipatterns, and we demonstrate how well a periodic pattern in a large domain can approximate a quasipattern.

In order to use triad interactions to encourage modes at 30°, we choose $m = 4$, $n = 5$ forcing: $4 : 5$ forcing has been used in several experiments to produce 12-fold quasipatterns [1, 20, 34]. We set $\hat{\Omega}(k = k_4 = 1) = 2$ so that the subharmonic response to frequency 4 comes at wavenumber 1, and we require that a wavenumber involved in 150° mode interactions ($k^2 = 2 - \sqrt{3}$) correspond to the difference frequency: $\hat{\Omega}(k) = 1$. One solution is $\omega = 0.633975$, $\beta = -1.366025$ and $\delta = 0$. Twelve-fold quasipatterns also require modes at 90° to be favoured, and for this choice of parameters, $\hat{\Omega}(k = \sqrt{2})$ is 3.37. Although this is not particularly close to 4, we can use $1 : 2$ resonance (driving at frequency 8) to control the 90° interaction. The linear theory for these cases is in figure 7.1, with $\mu = -0.2$, $\alpha = -0.2$ and $\gamma = -0.15$. Note that the damping is non-monotonic, and has a minimum at $k = 1$.

The resulting B_θ curve with $4 : 5 : 8$ forcing and with near-Hamiltonian choice of nonlinear coefficients (figure 7.2) shows pronounced dips at 30° and 90° as required. In figure 7.3, we show that within a 12-amplitude cubic truncation, 12-fold quasipatterns

are stable between 0.9995 and 1.0085 times critical. We have found stable approximate quasipatterns (marked by crosses on the figure, and discussed in more detail below) in the same range. Squares are also stable above 1.0013 times critical. The agreement is good, better than the examples in the previous section (figure 6.4), since the difference frequency mode is still fairly well damped (compare the damping for k close to 0.378 in figure 6.1f and $k = 0.518$ in figure 7.1f).

7.1. Choice of domain size for approximate quasipatterns. Before presenting numerical solutions in large domains, we discuss the issue of choice of domain for providing accurate approximations to quasipatterns.

Just as hexagonal patterns can be approximated in rectangular domains [39], there are many ways of choosing periodic domains to allow accurate approximations of quasipatterns. Here we discuss three plausible approaches to choosing domains for 12-fold quasipatterns. We show why one approach, based on Pythagorean triplets, does not work at all, while two other approaches both work well.

Reducible symmetry group representations with square periodic domains have been put forward as candidates for producing approximate quasipatterns [15, 59]. In particular, Pythagorean triplets have been identified as of particular interest in this case [15]. Consider a pair of integers (p, q) with $p > q > 0$. Then $(p^2-q^2, 2pq, p^2+q^2)$ forms a Pythagorean triplet (*i.e.*, $(p^2 - q^2)^2 + (2pq)^2 = (p^2 + q^2)^2$), and the vectors $\boldsymbol{k}^{(1)} = (1, 0)$ and $\boldsymbol{k}^{(2)} = (2pq, p^2 - q^2)/(p^2 + q^2)$ have the same length. For example, with $p = 7$, $q = 4$, we have $\boldsymbol{k}^{(1)} = (1, 0)$ and $\boldsymbol{k}^{(2)} = (\frac{56}{65}, \frac{33}{65})$. If $\frac{p}{q}$ is a continued fraction approximation of $\sqrt{3}$ (table 7.1), then the angle between these two vectors, namely $\tan^{-1}\left((p^2 - q^2)/(2pq)\right)$, tends to $30^\circ + \mathcal{O}(1/q^2)$ as the approximation to $\sqrt{3}$ improves. Thus it might be thought that square $(p^2 + q^2) \times (p^2 + q^2)$ domains might readily allow approximations to 12-fold quasipatterns.

Unfortunately, these Pythagorean domains do not provide good approximations to quasipatterns. The reason is that the essential 60° coupling is not quite correct: consider the wavevector $\boldsymbol{k}^{(1)} = (p^2 + q^2, 0)$ (in units of the basic lattice vector), and, at 60° on either side of $\boldsymbol{k}^{(1)}$, the wavevectors $\boldsymbol{k}^{(3)} = (p^2 - q^2, 2pq)$ and $\boldsymbol{k}^{(11)} = (p^2 - q^2, -2pq)$, where we number wavevectors anticlockwise from $\boldsymbol{k}^{(1)}$. In order for quadratic interactions between these three modes to occur, we need $\boldsymbol{k}^{(1)} = \boldsymbol{k}^{(3)} + \boldsymbol{k}^{(11)}$. However, in this case, $\boldsymbol{k}^{(3)} + \boldsymbol{k}^{(11)} = (2(p^2 - q^2), 0) = \boldsymbol{k}^{(1)} + (p^2 - 3q^2, 0)$, which is close to, but never equal to, $\boldsymbol{k}^{(1)}$: it can be shown that $p^2 - 3q^2 = 1$ or -2, which is small compared to $|\boldsymbol{k}^{(1)}| = p^2 + q^2$. This small difference means that the important nonlinear interactions between these three waves generate erroneous long-wave modulations in square $(p^2 + q^2) \times (p^2 + q^2)$ domains, and if modes with wavenumber close to zero are not heavily damped, these long-wave modulations can dominate the pattern.

A much better way of generating good approximations to 12-fold quasipatterns is to choose $2q \times 2q$ domains, with vectors $\boldsymbol{k}^{(1)} = (1, 0)$ and $\boldsymbol{k}^{(2)} = (p, q)/2q$, with $\frac{p}{q}$ drawn from table 7.1. Again, the angle between these vectors goes as $30^\circ + \mathcal{O}(1/q^2)$, and, though the wavenumbers are not quite equal, we have $|\boldsymbol{k}^{(2)}| \to 1 + \mathcal{O}(1/q^2)$.

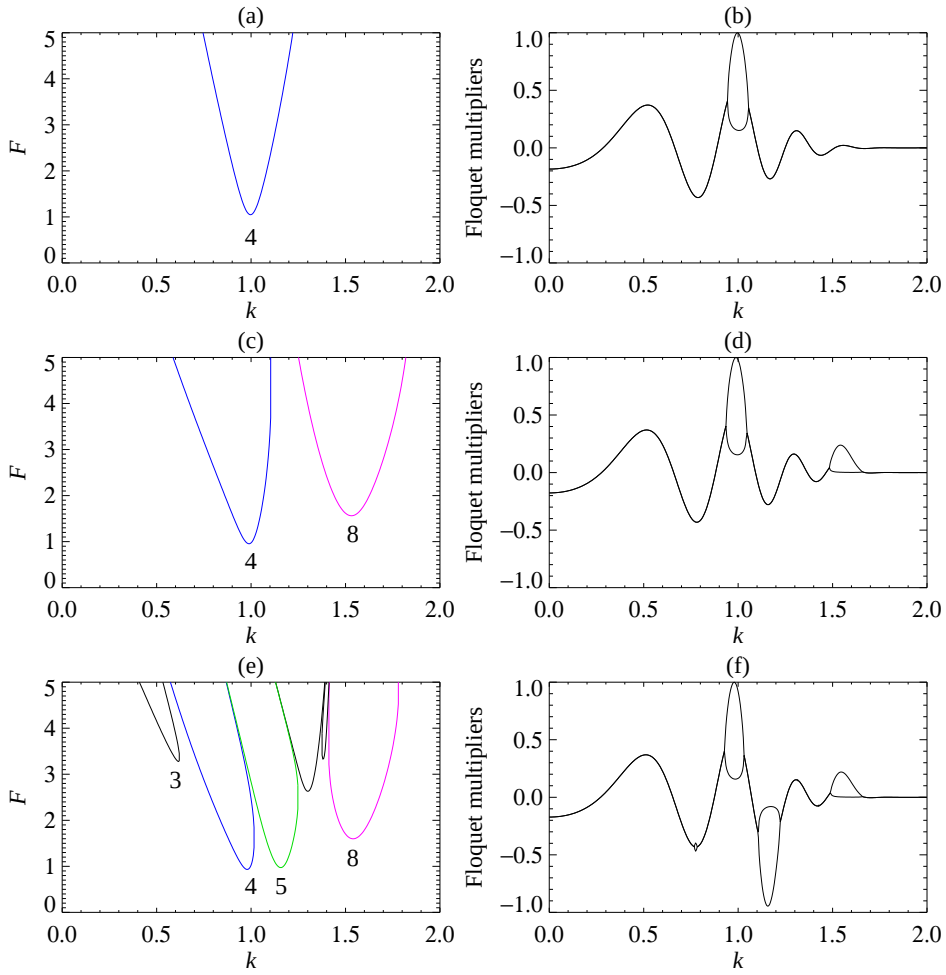

FIG. 7.1. *Linear theory for the quasipattern example. The dispersion relation coefficients are* $\omega = 0.633975$, $\beta = -1.366025$ *and* $\delta = 0$, *and the damping coefficients are* $\mu = -0.2$, $\alpha = -0.2$ *and* $\gamma = -0.15$. *(a,b)* 4 *forcing, with* $a_4 = 0.57358$ *and* $F_c = 1.04730$. *(c,d)* $4:8$ *forcing, with* $(a_4, a_8) = (0.57358, 1.6)$, $(\phi_4, \phi_8) = (0, 0)$ *and* $F_c = 0.95214$. *(e,f)* $4:5:8$ *forcing, with* $(a_4, a_5, a_8) = (0.57358, 0.81915, 1.6)$, $(\phi_4, \phi_5, \phi_8) = (0, 0, 0)$, $F_c = 0.93159$ *and* $k_c = 0.9798$. *(a,c,e) show neutral stability curves, whose minima define* F_c *and the critical wavenumber (close to 1 in all cases). The main harmonic curves are blue, subharmonic curves are green, and curves corresponding to response at twice the main forcing frequency are magenta, with the corresponding driving frequency indicated. (b,d,e) show the real parts of the Floquet multipliers at the critical forcing, confirming in (b) that the instability is harmonic (Floquet multiplier equal to one) at* $k = 1$, *in (d) that the modes corresponding to frequency* 8 *are not as strongly damped as in (b), and in (f) that modes with wavenumber close to* 0.518 *are relatively weakly damped (Floquet multiplier about* 0.5*) even though the difference frequency is not driven directly.*

$\frac{p}{q}$	$\frac{2}{1}, \frac{5}{3}, \frac{7}{4}, \frac{19}{11}, \frac{26}{15}, \frac{71}{41}, \frac{97}{56}, \frac{265}{153}, \frac{362}{209}, \cdots \to \sqrt{3}$

TABLE 7.1
Continued fraction approximations to $\sqrt{3}$.

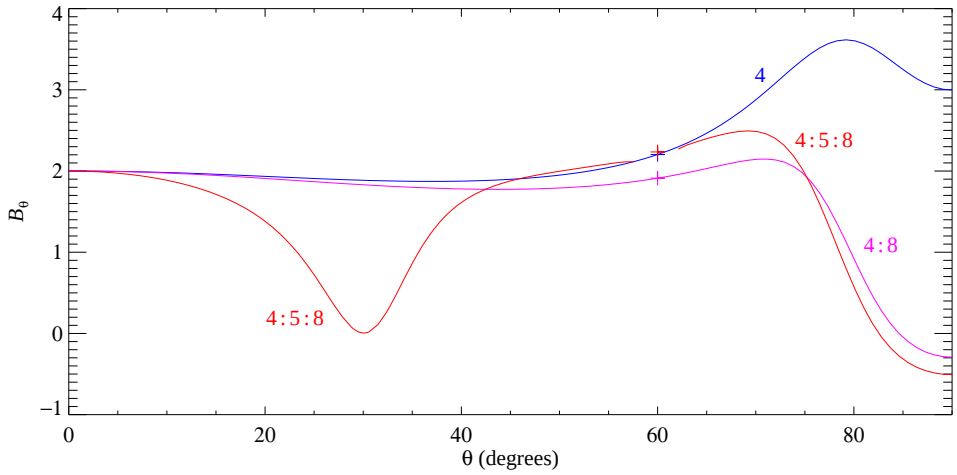

FIG. 7.2. *Cross-coupling coefficient B_θ for the parameters from figure 7.1 and nonlinear coefficients $Q_1 = 1+i$, $Q_2 = -2+2i$, $C = -1+10i$. The blue curve is with 4 forcing only: the peak near 80° is because of 1 : 2 resonance with frequency 8. The magenta curve has 4 : 8 forcing, using the frequency 8 component to bring down the curve close to 90°. Bringing in the 5 frequency (red curve) give a pronounced dip at 30°, corresponding to the difference frequency (5 − 4), even though this mode is not driven directly. The relevant coefficients are $B_{30} = -0.01$, $B_{60} = 2.24$ and $B_{90} = -0.51$.*

This approach works because with this choice of wavevectors, we do have the correct three-wave coupling: $\boldsymbol{k}^{(3)} = (q,p)/2q$, $\boldsymbol{k}^{(11)} = (q,-p)/2q$ and so $\boldsymbol{k}^{(3)} + \boldsymbol{k}^{(11)} = \boldsymbol{k}^{(1)}$.

A third possibility is to approximate the quasipattern as a superlattice pattern, using the 12-dimensional irreducible representations of $D_6 \ltimes T^2$ [18]. If we choose $\alpha = q$ and $\beta = p - q$ (in the notation of [18, table 2]), with $\frac{p}{q}$ drawn from table 7.1, then $\boldsymbol{k}^{(1)} = ((p-q)\sqrt{3}, 3q-p)$, $\boldsymbol{k}^{(2)} = ((2q-p)\sqrt{3}, p)$, $\boldsymbol{k}^{(3)} = ((p-2q)\sqrt{3}, p)$, $\boldsymbol{k}^{(11)} = ((q\sqrt{3}, 3q-2p)$ (all these should be divided by their length, $\sqrt{p^2-3pq+3q^2}$). We have $\boldsymbol{k}^{(3)} + \boldsymbol{k}^{(11)} = \boldsymbol{k}^{(1)}$ as required, all wavevectors are the same length (which is an advantage over the second alternative), and the angle between $\boldsymbol{k}^{(1)}$ and $\boldsymbol{k}^{(2)}$ goes as $30° + \mathcal{O}(1/q^2)$. One disadvantage of this approach is that numerical solutions of the PDE must be carried out in $2\sqrt{p^2-3pq+3q^2} \times 2\sqrt{(p^2-3pq+3q^2)/3}$ rectangular domains in order to take advantage of spectral numerical methods. These domains are big enough to contain two repeats of the pattern (as in figure 6.3b) and so only half the Fourier coefficients are used.

The last two methods are compared in table 7.2. The error between the approximation and the 12-fold quasipattern is inversely proportional to the area of the domain in both cases. The hexagonal superlattice approximations have all wavevectors of the correct length, unlike the square approximation. For this reason, the superlattice case is better for computing bifurcation diagrams, as all modes bifurcate at the same value of the forcing.

However, for similar domain areas, the angular separation between wavevectors is

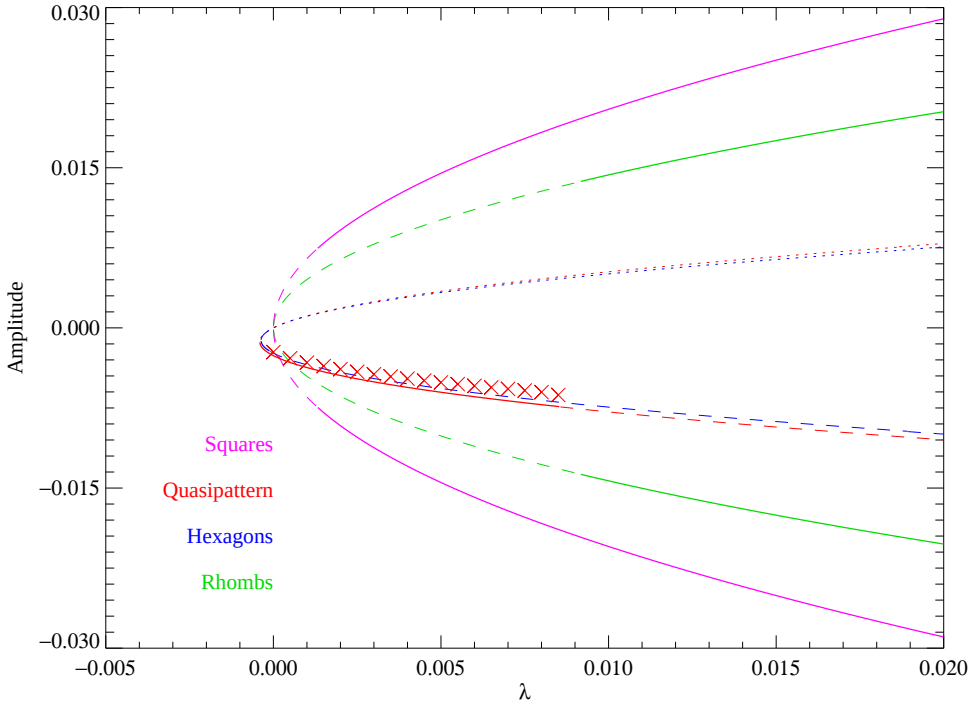

FIG. 7.3. *Bifurcation diagram with 3-frequency* 4 : 5 : 8 *forcing based on a 12-amplitude cubic truncation, with parameter values as in figure 7.2. 12-fold quasipatterns (red) are predicted to be stable up to* 1.0085 *times critical; squares (magenta) are stable from* 1.0013 *times critical and* 30° *rhombs (green) from* 1.0092 *times critical. The crosses show the amplitudes of stable approximate quasipattern solutions of the PDE, calculated in a domain* $2\sqrt{13} \times 2\sqrt{13/3}$ *critical wavelengths.*

about four times closer to 30° in the square case as compared to the superlattice case. Moreover, the square case is more amenable to efficient use of fast Fourier transforms, since the number of modes can be chosen to be a power of two in each direction, while the superlattice case leads to more awkward choices of numbers of modes.

For these reasons, we choose the rectangular $2\sqrt{13} \times 2\sqrt{13/3}$ domain for the bifurcation diagram in figure 7.3, since the quantitative comparison between numerical simulation and analysis is easier when all modes have the same wavenumber and hence bifurcate at the same value of the forcing (see below). We use the more convenient square (8×8, 30×30 and 112×112) domains for the remaining PDE simulations described below. It would be interesting to see how sensitive the quasipattern is to the exact choice of domain size. It would also be interesting to find domains that provide particularly accurate approximations to 8-, 10-, 14-fold and higher order quasipatterns, but these issues are beyond the scope of this paper.

One consequence of the wavevectors being of unequal length in the square case is that the two wavenumbers concerned have slightly different critical forcings. In

p/q	$A=$ Area	First two wavevectors	$(\lvert\boldsymbol{k}^{(2)}\rvert-1)A$	$(\angle_{12}-30^\circ)A$
$\frac{p}{q}$	$\frac{4(p^2-3pq+3q^2)}{\sqrt{3}}$	$\boldsymbol{k}^{(1)}=\frac{((p-q)\sqrt{3},3q-p)}{2\sqrt{p^2-3pq+3q^2}}$, $\boldsymbol{k}^{(2)}=\frac{((2q-p)\sqrt{3},p)}{2\sqrt{p^2-3pq+3q^2}}$		
$\frac{7}{4}$	30.02	$\frac{(3\sqrt{3},5)}{\sqrt{52}}$, $\frac{(\sqrt{3},7)}{\sqrt{52}}$	0	66.2
$\frac{19}{11}$	224.01	$\frac{(8\sqrt{3},14)}{\sqrt{338}}$, $\frac{(3\sqrt{3},19)}{\sqrt{338}}$	0	−132.3
$\frac{26}{15}$	418.00	$\frac{(11\sqrt{3},19)}{\sqrt{724}}$, $\frac{(4\sqrt{3},26)}{\sqrt{724}}$	0	66.2
$\frac{71}{41}$	3120.0	$\frac{(30\sqrt{3},52)}{\sqrt{5404}}$, $\frac{(11\sqrt{3},71)}{\sqrt{5404}}$	0	−132.3
$\frac{97}{56}$	5822.0	$\frac{(41\sqrt{3},71)}{\sqrt{10084}}$, $\frac{(15\sqrt{3},97)}{\sqrt{10084}}$	0	66.2
⋮				
$\sqrt{3}$	∞	$\frac{(1,1)}{\sqrt{2}}$, $\frac{(\sqrt{3}-1,\sqrt{3}+1)}{2\sqrt{2}}$		
$\frac{p}{q}$	$2q\times 2q$	$\boldsymbol{k}^{(2)}=\left(\frac{p}{2q},\frac{1}{2}\right)$		
$\frac{7}{4}$	64	$\boldsymbol{k}^{(2)}=\left(\frac{7}{8},\frac{1}{2}\right)$	0.498	−16.3
$\frac{19}{11}$	484	$\boldsymbol{k}^{(2)}=\left(\frac{19}{22},\frac{1}{2}\right)$	−1.001	33.2
$\frac{26}{15}$	900	$\boldsymbol{k}^{(2)}=\left(\frac{26}{30},\frac{1}{2}\right)$	0.500	−16.5
$\frac{71}{41}$	6724	$\boldsymbol{k}^{(2)}=\left(\frac{71}{82},\frac{1}{2}\right)$	−1.000	33.1
$\frac{97}{56}$	12544	$\boldsymbol{k}^{(2)}=\left(\frac{97}{112},\frac{1}{2}\right)$	0.500	−16.5
⋮				
$\sqrt{3}$	∞	$\boldsymbol{k}^{(2)}=\left(\frac{\sqrt{3}}{2},\frac{1}{2}\right)$		

TABLE 7.2

Domains that provide good approximations to 12-fold quasipatterns. The first column gives the rational number $\frac{p}{q}$ that is a continued fraction approximation to $\sqrt{3}$, drawn from table 7.1. The second and third columns give the area of a computational domain and two of the wavevectors that will make up an approximate quasipattern. The fourth and fifth columns demonstrate that the errors in the length of $\boldsymbol{k}^{(2)}$ and in the angle $\angle_{12}$ between $\boldsymbol{k}^{(1)}$ and $\boldsymbol{k}^{(2)}$ scale as $1/A$, or equivalently, as q^{-2}. The first set of rows refer to rectangular domains of size $2\sqrt{p^2-3pq+3q^2}\times 2\sqrt{(p^2-3pq+3q^2)/3}$, which allow superlattice patterns that approximate quasipatterns. In these examples, all wavevectors are the same length. The second set of rows refer to square domains of size $2q\times 2q$. In these domains, approximate quasipatterns have wavevectors that have two slightly different lengths, with one wavevector being $\boldsymbol{k}^{(1)}=(1,0)$.

the 30×30 and 112×112 cases, this difference is negligible, but in the 8×8 case, the critical forcings for the two wavenumbers are appreciably different. We therefore make a small adjustment to the domain size to make the two critical forcings the same, raised by a factor of 1.00066 above F_c.

7.2. Numerical examples of 12-fold quasipatterns. Numerical solutions of the PDE (3.1) with $4:5:8$ forcing at 1.003 times critical are shown in figure 7.4, in periodic domains 8×8, 30×30 and 112×112 wavelengths with periodic boundary conditions and using up to 1536^2 Fourier modes. The solutions were followed for at

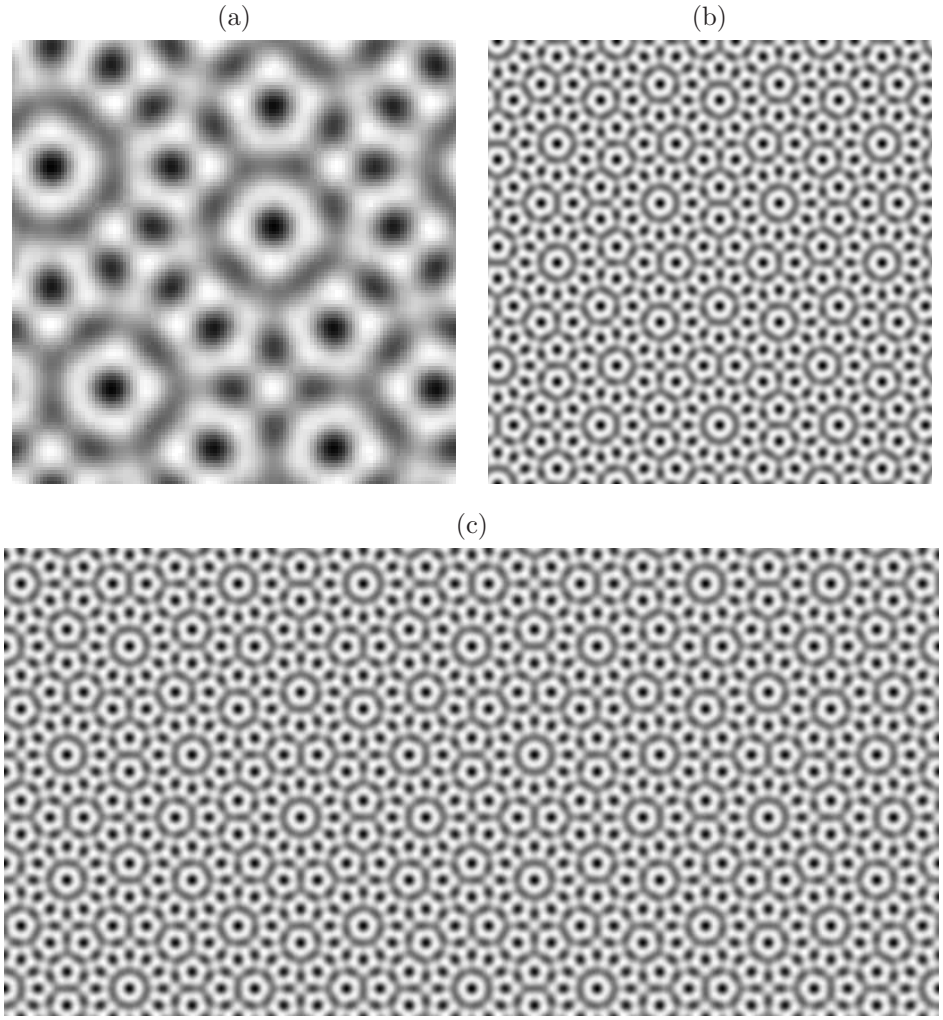

FIG. 7.4. *Numerical solutions of the PDE with* $4:5:8$ *forcing at* 1.003 *times critical. (a)* 8×8 *domain. (b)* 30×30 *domain. (c)* 112×112 *domain (only a* 60×30 *section of the domain is shown). Parameter values are as in figure 7.2.*

least 10 000 forcing periods in the largest domain. Most initial conditions resulted in square patterns, but minor adjustments to the Fourier amplitudes at an early stage of the calculation resulted in stable approximate 12-fold quasipatterns. Note, however, that the PDE solutions in figure 7.4 were not constrained to choose exactly the wavevectors given in table 7.2.

The accuracy of the approximation improves with increasing domain size. The modes involved in the 30×30 example are $(30,0)$ and $(26,15)$ and their reflections, which are 29.98° apart, and differ in length by 0.05%. The larger 112×112 domain allows an improved approximation to the quasipattern: the important wavevectors are $(112,0)$ and $(97,56)$, which are 29.9987° apart and differ in length by 0.004%.

The amplitudes of these modes differ by 1%. We discuss other ways of evaluating the improved approximation to quasiperiodicity in the next section.

7.3. Fourier spectra of quasipatterns. All the numerical PDE solutions presented here have been carried out in periodic domains, so these solutions are only approximations to quasipatterns. In the 12-fold examples (figures 7.4 and 8.3a below), the most important twelve wavevectors in the pattern are not exactly 30° apart and do not have exactly the same length (see table 7.2). On the other hand, it is possible to generate true quasipatterns using twelve modes with $k = 1$ evenly spaced around the unit circle, but the asymptotic series in the weakly nonlinear approximation are known to diverge [52]. In this section, we compare the detailed Fourier spectra of the approximate quasipatterns to see how these differ from the spectra of true quasipatterns.

We make the comparison by computing the locations of modes generated by nonlinear interactions up to a certain order, in the three cases of approximate quasipatterns in figure 7.4, as well as in a true quasipattern. To do this, we first define the *order* of a mode.

Quadratic interactions between the twelve modes with wavevectors $\boldsymbol{k}^{(1)}, \ldots, \boldsymbol{k}^{(12)}$ generate new modes with wavevectors $2\boldsymbol{k}^{(1)}$, $\boldsymbol{k}^{(1)}+\boldsymbol{k}^{(2)}$, $\boldsymbol{k}^{(1)}+\boldsymbol{k}^{(3)}$ and so on. Likewise, higher order nonlinear interactions between the twelve modes generate modes with wavevectors $\boldsymbol{k}^{(\boldsymbol{m})}$:

$$\boldsymbol{k}^{(\boldsymbol{m})} = \sum_{j=1}^{12} m_j \boldsymbol{k}^{(j)}, \tag{7.1}$$

where the m_j's are non-negative integers adding up to the *order* of the nonlinear interaction $|\boldsymbol{m}|$, defined by $|\boldsymbol{m}| = \sum_{j=1}^{12} m_j$. In the case of a periodic domain, the set of all possible $\boldsymbol{k}^{(\boldsymbol{m})}$ defines a lattice of wavevectors (figure 5.1a,b), while in the quasipattern case, the set of all possible $\boldsymbol{k}^{(\boldsymbol{m})}$ defines a *quasilattice*: examples of 12- and 14-fold quasilattices with $|\boldsymbol{m}| \le 11$ ($|\boldsymbol{m}| \le 7$ in the 14-fold case) are shown in figure 5.1(c,d). If a wavevector $\boldsymbol{k}$ is in the lattice or quasilattice, then $\boldsymbol{k} = \boldsymbol{k}^{(\boldsymbol{m})}$ for an infinite number of choices of vector $\boldsymbol{m}$ (corresponding to nonlinear interactions of differents orders), since increasing m_1 and m_7 (say) by the same amount does not change $\boldsymbol{k}^{(\boldsymbol{m})}$ but increases $|\boldsymbol{m}|$ by 2. We define the *order* of wavevector $\boldsymbol{k}$ to be the smallest value of $|\boldsymbol{m}|$ with $\boldsymbol{k}^{(\boldsymbol{m})} = \boldsymbol{k}$.

In figures 7.5 and 7.6 we compare the locations of wavevectors in the 8×8 (cyan), 30×30 (blue) and 112×112 (red) examples from the simulation results shown in figure 7.4. The 8×8 spectrum is only in figure 7.5(a) (up to 7th order), and the 30×30 spectra are only up to 26th order. The amplitudes of each Fourier mode is given by the size of the symbol (on a logarithmic scale): the largest symbols are the modes with the largest amplitudes, and the modes with the smallest symbols have amplitudes 10^{17} times smaller. Modes with amplitudes smaller than this are not plotted as these are in the realm of round-off error (see below).

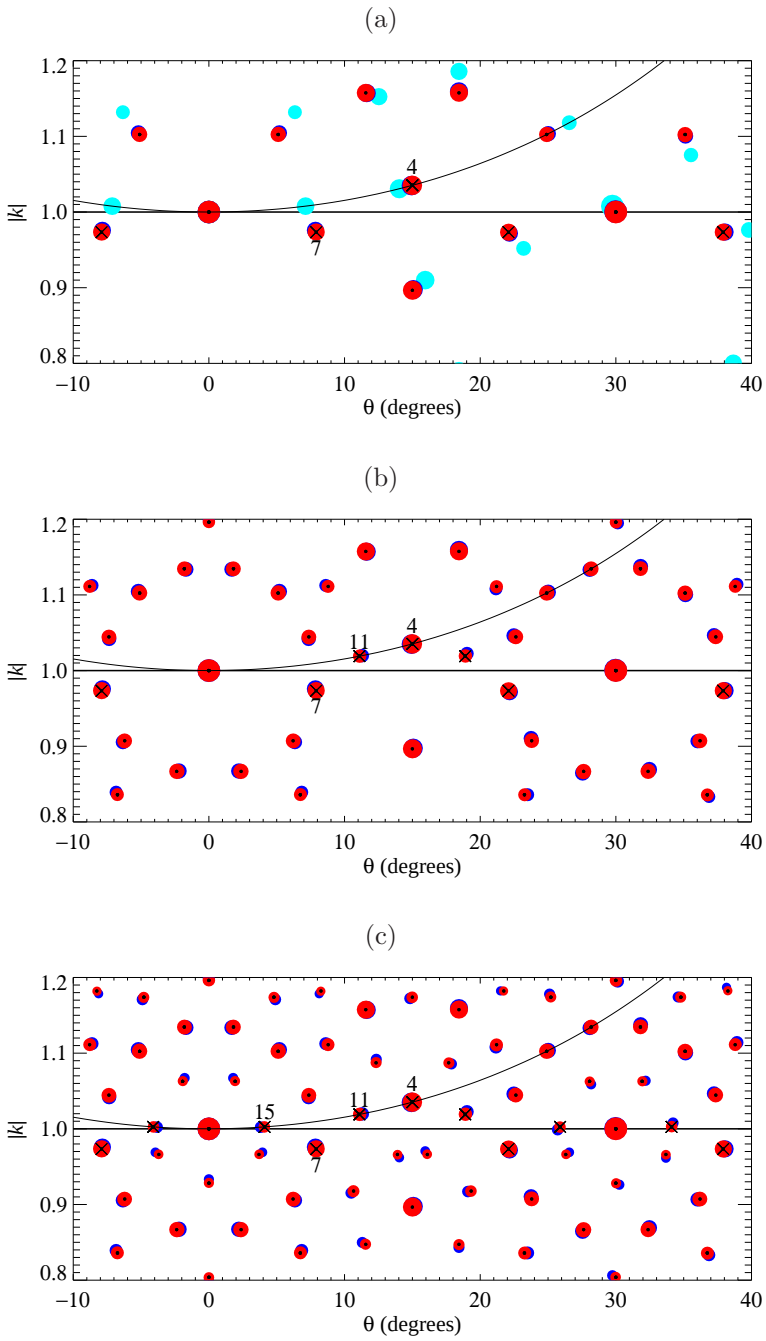

FIG. 7.5. *Fourier spectra of* 8×8 *(cyan),* 30×30 *(blue),* 112×112 *(red) approximate 12-fold quasipatterns, as well as the 12-fold quasilattice (small black dots), up to (a) 7th, (b) 11th and (c) 15th order. The size of the coloured marker indicates the amplitude of the corresponding Fourier mode on a logarithmic scale, with the smallest markers having* 10^{17} *times smaller amplitude than the largest. Only Fourier modes close to the unit circle (*$0.8 \le |\boldsymbol{k}| \le 1.2$*) are shown, with wavevector angles* $-10° \le \theta \le 40°$*. The horizontal line* $k = 1$ *represents the unit circle, while the curved line represents* $k_x = 1$*. Wavevectors that come closest to the unit circle up to a particular order are labelled with* $\times$*.*

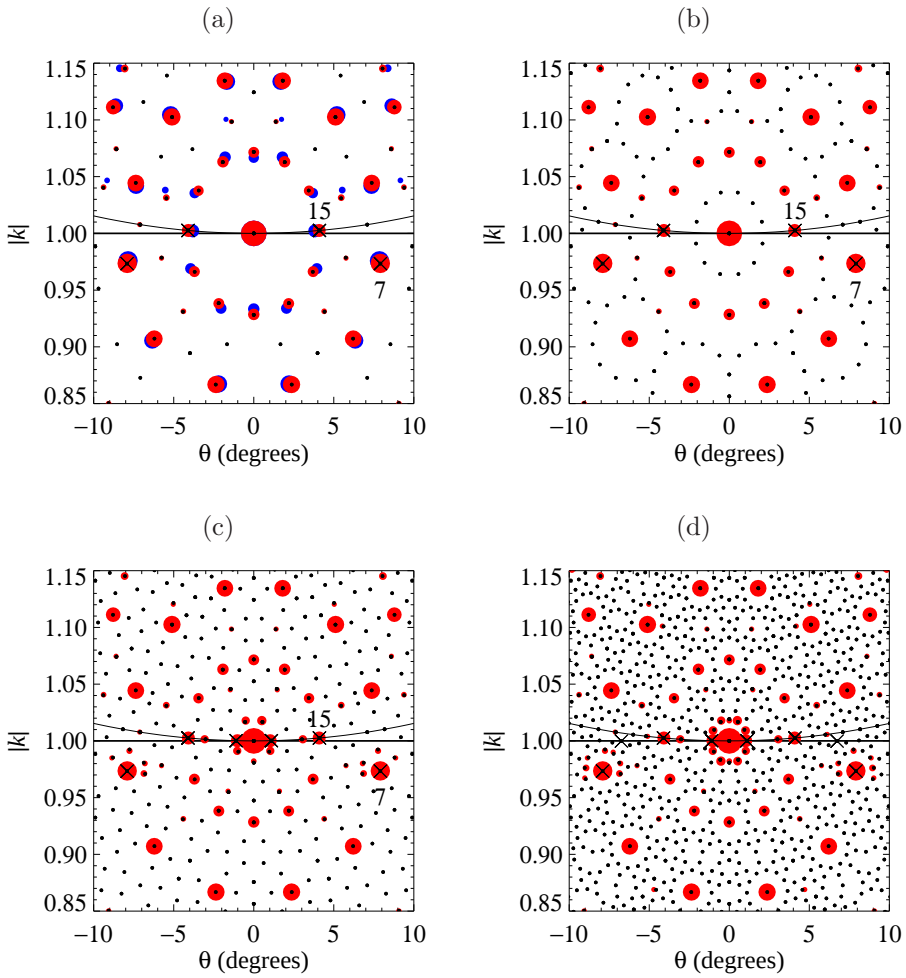

FIG. 7.6. *Fourier spectra of* 30×30 *(blue) and* 112×112 *(red) approximate 12-fold quasipatterns, as well as the 12-fold quasilattice (small black dots), up to (a) 26th, (b) 39th, (c) 56th and (d) 94th order. Here we show wavevectors within* $10°$ *of* $(1,0)$*, and with* $0.85 \le |\boldsymbol{k}| \le 1.15$.

The success with which the periodic patterns approximate a true quasipattern can be judged by the locations of the important modes in the pattern, as compared to the locations of modes on the quasilattice, up to a given order. Up to 7th order (figure 7.5a), the 30×30 and 112×112 modes (blue and red) overlay each other almost exactly, and correspond well with the quasilattice modes (small black dots at the centre of the red markers). However, the 8×8 modes (cyan) deviate substantially from the correct locations, and we conclude that the periodic pattern in an 8×8 domain is a poor approximation to a quasipattern (in spite of appearances in figure 7.4a).

At 11th order (figure 7.5b), the agreement between 30×30, 112×112 and the true quasipattern is still good, while at 15th order (figure 7.5c), the 30×30 modes deviate noticeably from the 112×112 and quasipattern modes. This is more pronounced at

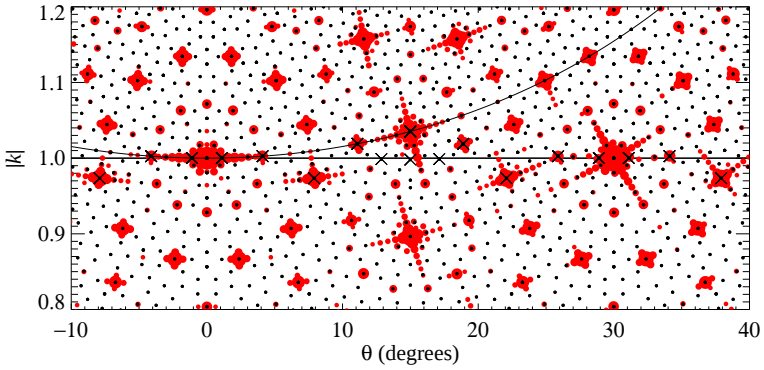

FIG. 7.7. *Fourier spectra of the* 112×112 *(red) approximate 12-fold quasipattern, as well as the 12-fold quasilattice (small black dots). All modes with amplitude greater than* 10^{-17} *times the maximum amplitude are plotted; the quasilattice is plotted up to 56th order. The competing effects of the 12-fold order and the square lattice are apparent.*

26th order (figure 7.6a).

At 15th order (figure 7.5c), the agreement between 112×112 and the true quasipattern is excellent: every red marker has a black dot at its centre. The agreement is still very good at 26th order (figure 7.6a): the black dots are not quite in the centres of the smallest red markers, and some black dots do not have corresponding red markers. This means that those modes, present in the true quasipattern at this order, have amplitudes in the 112×112 approximation that are too small to be plotted. The situation at 39th order (figure 7.6b) is similar, but it isn't until 94th order (figure 7.6d) that the true quasipattern modes miss the centres of the red markers entirely.

In fact, a curious situation arises at 56th and 94th order: it is apparent that modes close to $\boldsymbol{k} = (1, 0)$, and in particular modes on the line $k_x = 1$, have amplitudes that are higher than might be expected, since usually the amplitudes of modes decreases with their order. These modes are discussed in more detail below. However, it should be noted that plotting only modes up to a certain order masks the effect of the underlying lattice in the numerical solutions. In figure 7.7, we show all modes in the 112×112 down to round-off error, and quasilattice modes up to 56th order. The underlying square numerical lattice is clearly seen in the strings of red markers emanating from each large-amplitude mode. These give an impression that the large-amplitude modes could be considered to be clusters of modes in Fourier space.

In figure 7.8, we show the range of amplitudes of the modes as a function of order, for the 8×8, 30×30 and 112×112 approximate quasipatterns. We note that the 8×8 example deviates significantly from the other two at all orders, while the 30×30 and 112×112 examples are in fairly good agreement until 19th order or so, another indication of how the approximation improves with the domain size. We note that direct comparisons between the 8×8 case and the other two cases are not strictly valid, as the domain size in the 8×8 case had to be adjusted slightly to allow for the

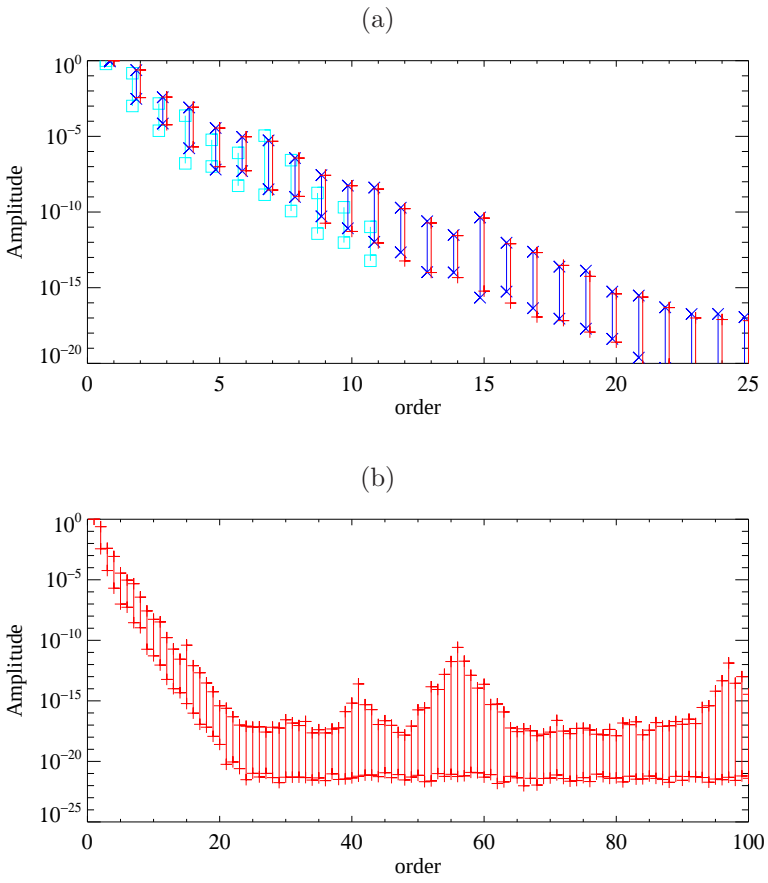

FIG. 7.8. *Fourier spectra of* 8×8 *(cyan),* 30×30 *(blue) and* 112×112 *(red) approximate 12-fold quasipatterns, as a function of order, (a) up to 25th order, (b) up to 100th order (*112×112 *only). The vertical lines indicate the range of amplitudes of modes at that order, scaled to the maximum amplitude at order 1.*

different wavenumbers in the pattern, as discussed above.

Figure 7.8(b) shows the spectrum of the 112×112 example at all orders up to 100. The range of amplitudes at a given order decays exponentially with order up to about 23rd order, but then levels off at the level of the round-off error: about 10^{-17}. On top of this pattern, there is a peak in amplitude at 15th order, and broad peaks around 41st, 56th and 97th order. We attribute these to the presence of weakly damped modes, with $\boldsymbol{k}$ close to unity, that appear around these orders. With weak damping, these modes will amplify the numerical noise in the PDE solutions, and nonlinear coupling implies that the amplified noise will feed in to nearby modes.

This is shown in figure 7.9, where we plot $\left||\boldsymbol{k}^{(\boldsymbol{m})}|-1\right|$ as a function of order $|\boldsymbol{m}|$ for the different examples. We note the marked drop in this quantity in particular at 15th and 39th order. While the drops in $\left||\boldsymbol{k}^{(\boldsymbol{m})}|-1\right|$ do not line up exactly with the peaks in amplitude, we suspect that it is this marked change in the damping of

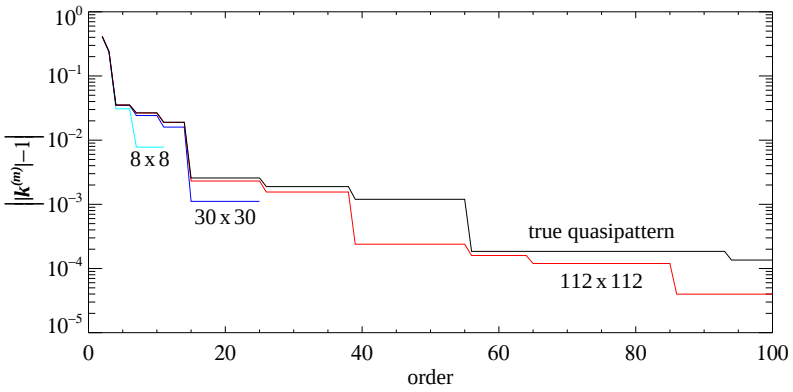

FIG. 7.9. *Minimum value of* $\left||\boldsymbol{k}^{(\boldsymbol{m})}|-1\right|$, *as a function of order* $|\boldsymbol{m}|$, *for* 8×8 *(cyan),* 30×30 *(blue),* 112×112 *(red) approximate 12-fold quasipatterns, and for a true 12-fold quasipattern (black) [52]. There are drops in this minimum quantity at 4th, 7th, 11th, 15th, 26th, 39th and 56th order in all cases. Modes that are responsible for these drops are identified in figures 7.5 and 7.6. In the* 30×30 *case, the Pythagorean mode* $(0.6, 0.8)$ *(which is of unit length) is generated at 26th order, which is why that curve terminates. The* 8×8 *curve continues horizontally.*

modes appearing at these orders that is responsible for the amplification of noise at around the same order.

Of course, for the numerical patterns in periodic domains, there is a lower bound to $\left||\boldsymbol{k}^{(\boldsymbol{m})}|-1\right|$ that does not depend on $|\boldsymbol{m}|$ (this lower bound is captured within figure 7.9), while for the true 12-fold quasipattern, there is no lower bound. If $|\boldsymbol{k}^{(\boldsymbol{m})}|\neq 1$, then

$$\left||\boldsymbol{k}^{(\boldsymbol{m})}|-1\right| > \frac{B}{|\boldsymbol{m}|^2}, \tag{7.2}$$

where B is an order-one constant [52]. For some particular choices of wavevectors, this asymptotic limit is achieved: for example, if

$$\boldsymbol{k}^{(\boldsymbol{m})} = p\boldsymbol{k}^{(4)} + (q-1)\boldsymbol{k}^{(9)} + (q+1)\boldsymbol{k}^{(11)} = (1, p-\sqrt{3}q), \tag{7.3}$$

where p and q are integers, then $|\boldsymbol{m}| = p+2q$ and $\left|\boldsymbol{k}^{(\boldsymbol{m})}\right|^2 = 1+(p-\sqrt{3}q)^2$. When $\frac{p}{q}$ is a continued fraction approximation to $\sqrt{3}$ (table 7.1), then $\left||\boldsymbol{k}^{(\boldsymbol{m})}|-1\right| \sim \frac{1}{2}(p-\sqrt{3}q)^2 \leq \frac{B_2}{q^2}$, so $\left||\boldsymbol{k}^{(\boldsymbol{m})}|-1\right| \leq \frac{B'}{|\boldsymbol{m}|^2}$, where B_2 and B' are order-one constants [52]. These particular vectors are not always the closest ones that can be found at a given order, but they demonstrate that modes approach the unit circle arbitrarily closely (and so are arbitrarily weakly damped) as the order of the mode increases. For the fractions listed in table 7.1, we have $|\boldsymbol{m}| = p+2q = 4, 11, 15, 41, 56, 153, \ldots$, but in fact there are step decreases in the minimum of $\left||\boldsymbol{k}^{(\boldsymbol{m})}|-1\right|$ at $|\boldsymbol{m}| = 4, 7, 11, 15, 26, 39, 56, 94$. This is the reason for the choices of orders in figures 7.5 and 7.6.

In summary, having identified which sizes result in the most accurate approximations to 12-fold quasipatterns, we find that in the largest example (112×112), the

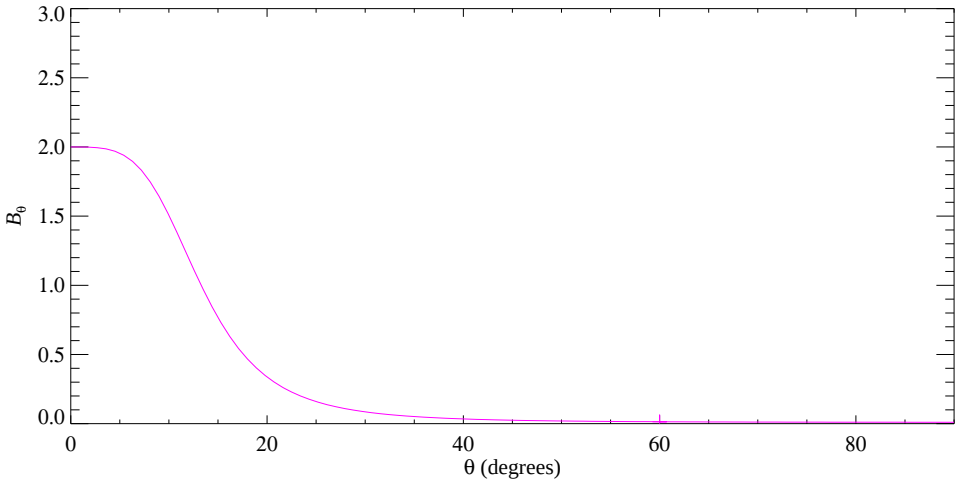

FIG. 8.1. *Cross-coupling coefficient B_θ for single frequency forcing, with $1:2$ resonance in space and time: $\omega = \frac{1}{3}$, $\beta = -\frac{1}{6}$, $\delta = 0$, $\mu = -0.005$, $\alpha = 0.001$, $\gamma = 0$, $Q_1 = 3 + 4i$, $Q_2 = -6 + 8i$, $C = -1 + 10i$, $F_c = 0.024002$ and $k_c = 0.9999$. Note that B_θ drops away sharply as θ increases, and is close to zero for $\theta \geq 30°$. The relevant coefficients are $B_{30} = 0.088$, $B_{60} = 0.014$ and $B_{90} = 0.010$.*

locations of the Fourier modes of the approximation deviate significantly from those of the true quasipattern only beyond 26th order. At this point, the amplitudes of the modes have reached the level of numerical round-off, so going any larger than 112×112 would not lead to any significant improvement in the approximation to a true quasipattern for these parameter values. The small divisors reveal themselves by amplifying the amplitudes of the Fourier modes at (or close to) the order at which the small divisor appears, but they do not appear to cause the amplitudes of the Fourier modes to become excessively large, at least at this level of forcing, and up to the maximum order (153) available in this domain.

8. Turbulent crystals: quasipatterns using $1:2$ resonance. In order to have $1:2$ resonance in space and time with single frequency forcing ($m = 1$), we impose $\hat{\Omega}(1) = \frac{1}{2}$ and $\hat{\Omega}(2) = 1$, which leads to $\omega = \frac{1}{3} + 4\delta$ and $\beta = -\frac{1}{6} + 5\delta$. We choose $\delta = 0$, small values for the damping coefficients μ, α and γ, and order one values for the nonlinear coefficients close to the Hamiltonian limit. The resulting cross-coupling curve is shown in figure 8.1: as explained in section 2, the $1:2$ resonance in space and time has enhanced the self-coupling coefficient (by about four orders of magnitude compared to the previous cases), and so the cross-coupling coefficient B_θ drops away sharply, and is close to zero for $\theta \geq 30°$.

Within the restrictions of a 12-mode expansion, 12-fold quasipatterns are stable (figure 8.2). Indeed, at 1.1 times the critical forcing, in a 30×30 domain, the numerical solution of the PDE with random initial conditions is a stable 12-fold approximate quasipattern (figure 8.3a). As above, the primary modes that make up the pattern

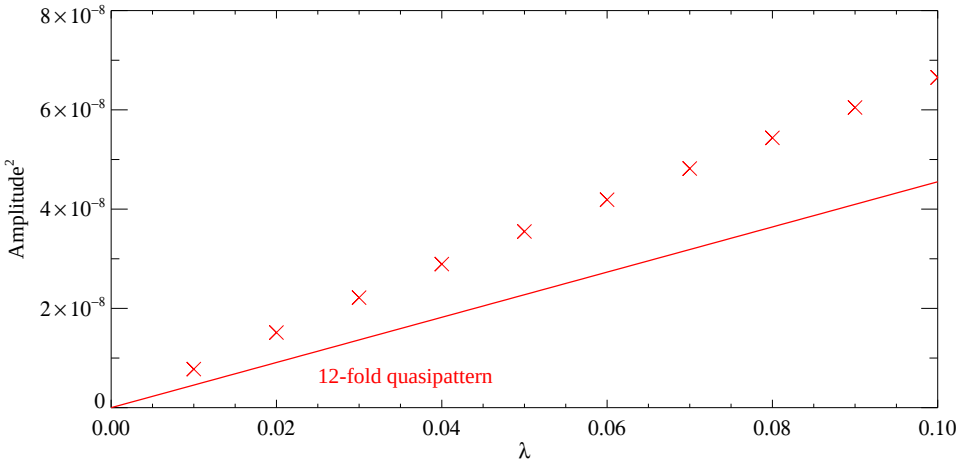

FIG. 8.2. *Bifurcation diagram showing the weakly nonlinear predicted amplitude (solid line) and amplitudes of approximate quasipattern solutions of the PDEs in an* 8×8 *domain (crosses).*

are $(30, 0)$ and $(26, 15)$ and their reflections, in units of basic lattice vectors. The amplitudes of the 12 modes differ by 0.5%. The initial condition was not in any invariant subspace, and the PDE was integrated for 160 000 periods of the forcing. The agreement between the weakly nonlinear predictions and the computed amplitudes is not good (figure 8.2), which we expect since the $k = 2$ mode is weakly damped (see discussion above).

However, there is no feature in the cross-coupling curve (figure 8.1) to indicate that modes at 30° should enjoy a special status. When the forcing is changed to 1.3 times critical with this 12-fold quasipattern as the initial condition, we find that it is unstable, and is replaced (after a transient of 70 000 periods) by a stable approximate 14-fold quasipattern (figures 8.3b and 8.4, and animation online). In this case, the 14 modes are $(30, 0)$, $(27, 13)$, $(19, 23)$, $(7, 29)$ and their reflections, differing in length by 0.5% and having angular separation within 1.5° of 360°/14, with spacings ranging from 24.7° to 27.1°. The amplitudes differ by about 10%. Both the 12-fold and 14-fold quasipatterns are stable at 1.2 times critical, in a 30×30 domain.

More complex quasipatterns are also possible: calculations done in larger 60×60 and 90×90 domains at 1.3 times critical, starting with random initial conditions, both yield approximate 20-fold quasipatterns (figure 8.3c). However, these are not a particularly accurate approximations to 20-fold quasipatterns: in the 60×60 case, the 20 modes are $(60, 0)$, $(58, 15)$, $(48, 36)$, $(, 53)$, $(21, 56)$, $(1, 60)$, $(-18, 57)$, $(-33, 50)$, $(-47, 37)$, $(-56, 21)$ and their 180° rotations, which differ in length by 0.4% and which have angular separations within 3° of 360°/20, with spacings ranging from 14.9° to 20.5°. The amplitudes of the 20 modes differ by up to 40%. Figure 8.5 shows an examination of the Fourier spectrum of figure 8.3(c): there are 20 peaks close to $k = 1$, of similar amplitudes and arranged roughly evenly around the unit

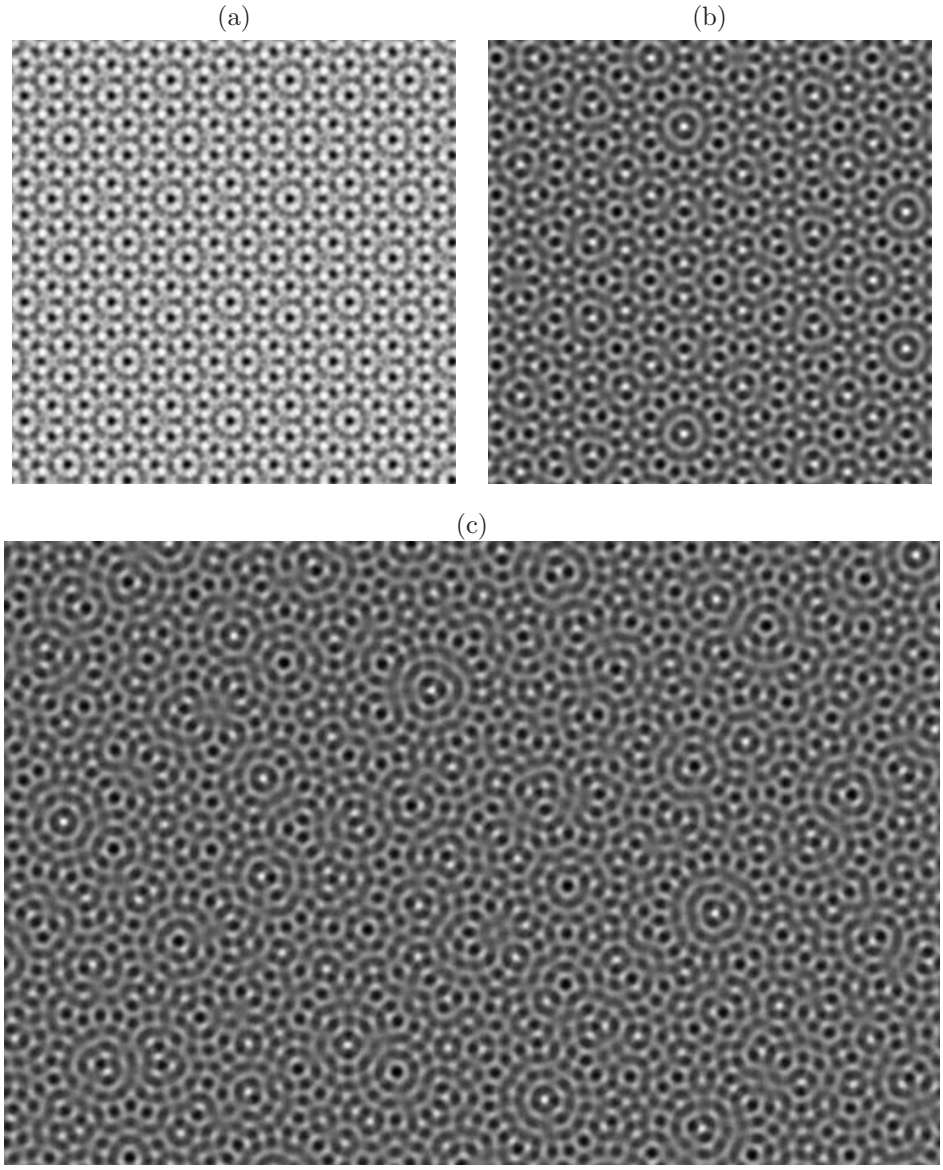

FIG. 8.3. *For the parameter values from figure 8.1, we find three different approximate quasipatterns depending on the amplitude of the forcing and the size of the domain. (a) 1.1 times critical,* 30×30 *domain: a 12-fold quasipattern. (b) 1.3 times critical,* 30×30 *domain: a 14-fold quasipattern. (c) 1.3 times critical,* 60×60 *domain: a 20-fold quasipattern (only* $\frac{2}{3}$ *of the domain is shown). An animation of the transition from (a) to (b), also showing details of the Fourier spectrum, can be found online.*

circle. The 90×90 example is similar: the 20 modes differ in length by 0.2% and also have angular separations within 3° of 360°/20, with spacings ranging from 15.0° to 20.7°. At 1.1 times critical in a 60×60 domain, we have also found a less accurate approximation to a 16-fold quasipattern: the 16 wavevectors differ in length by 0.3%,

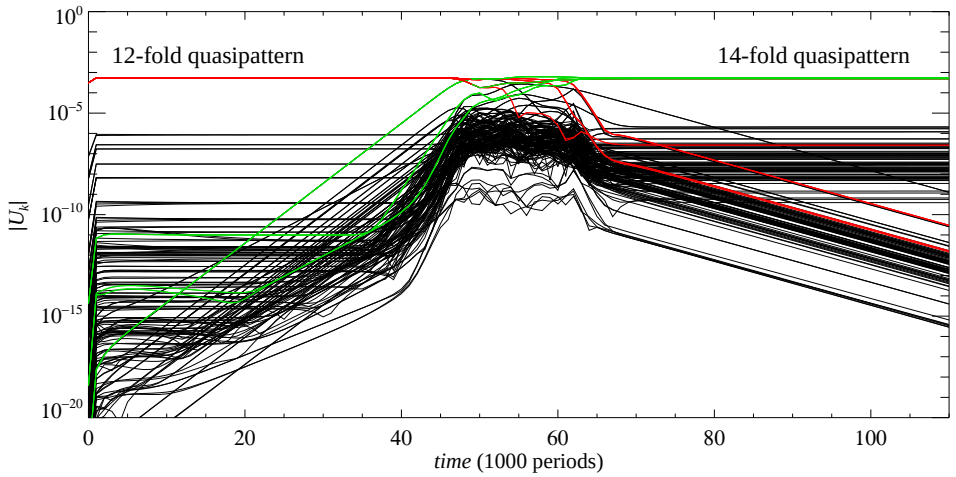

FIG. 8.4. *Amplitudes of Fourier modes as a function of time, at 1.3 times critical in a* 30×30 *domain. The initial condition was the 12-fold quasipattern from 1.1 times critical (red). This is unstable and, after an extended transient of* 70 000 *periods, it is replaced by the 14-fold quasipattern (green). Amplitudes of other Fourier modes close to* $k = 1$ *are shown in black. An animation of this transition can be found online.*

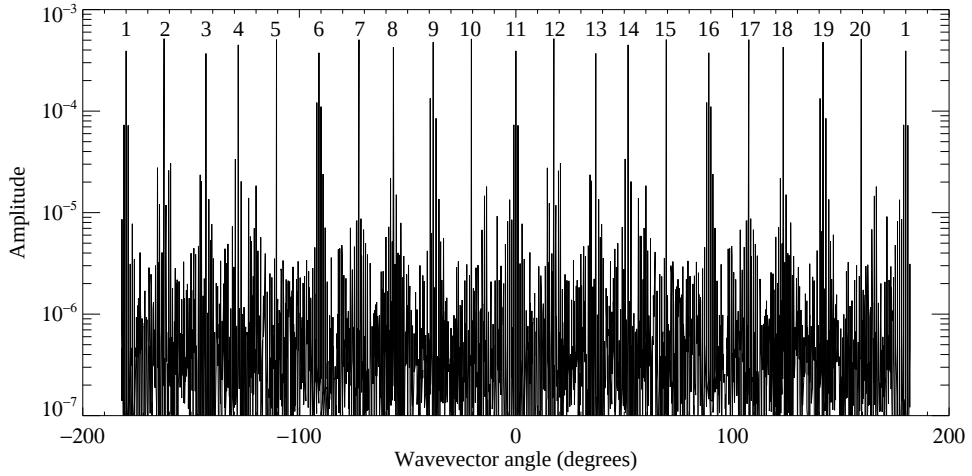

FIG. 8.5. *Amplitudes of Fourier modes of the 20-fold quasipattern from figure 8.3(c), as a function of wavevector orientation, for* $0.95 \le |\boldsymbol{k}| \le 1.05$*, showing twenty peaks roughly evenly distributed.*

with spacings ranging from 14.5° to 27.8°. We speculate that in other domains and at other forcings, 18-fold and indeed other approximate quasipatterns could also be observed.

The cross-coupling B_θ curve suggests that modes that are more than about 30° apart do not influence each other (at least in an amplitude equation truncated at cubic order). This suggests that patterns containing many modes at essentially arbitrary an-

gles might be expected – such patterns have been termed *turbulent crystals* by Newell and Pomeau [46]. It is hard to see why one quasipattern should be favoured over another, or indeed, why quasipatterns (with wavevectors evenly distributed around the $k = 1$ circle) should be favoured over more complex patterns.

We have not attempted to compare the locations of the high-order modes in these 14- and 20-fold approximate quasipatterns with those in the true quasipatterns, as these higher quasilattices are very densely populated (figure 5.1d), and the approximate solutions are not close enough to the true quasipatterns.

As an aside, there is an interesting connection that can be made between the Fourier spectra of these high-order quasipatterns and the fractal dynamics of the complex ODE $d^2\zeta/dt^2 = -\zeta^{Q-1}$, where Q is an even integer [26]. Solutions of this equation lie on multiply branched Riemann surfaces, with branch points occurring densely at points in a Q-fold quasilattice.

The rotational degeneracy of the plane (in the absence of boundary conditions) implies that any mode with $|\boldsymbol{k}| = 1$ is linearly excited, and it is an open question as to why patterns and quasipatterns, with a finite number of modes evenly distributed around the unit circle, should be the preferred patterns close to onset in so many examples of pattern-forming systems. (Of course, pattern-forming systems are by definition those that produce regular patterns close to onset!) Newell and Pomeau [46] wrote down the evolution equation of Q modes, ignoring quadratic terms (which are absent in the case of subharmonic waves) and truncating at cubic order:

$$\frac{dA_j}{dt} = \lambda A_j - \sum_{k=1}^{Q} B_{\theta_{jk}} |A_k|^2 A_j, \tag{8.1}$$

where A_j is the complex amplitude of mode j ($j = 1, \ldots, Q$), λ is the growth rate, and θ_{jk} is the angle between the wavevectors of modes j and k. Truncated in this way, the phases of the amplitudes do not enter the dynamics: Newell and Pomeau [46] attribute this to the translation symmetry of the underlying problem, but Melbourne [41] points out that this phase-invariance is in fact a normal form symmetry and hence not exact.

This system of ODEs is variational, and evolves to minimise a free energy

$$\mathcal{F} = -\lambda \sum_{j=1}^{Q} |A_j|^2 + \frac{1}{2} \sum_{j,k=1}^{Q} B_{\theta_{jk}} |A_j|^2 |A_k|^2. \tag{8.2}$$

Newell and Pomeau [46] claim that in the case that the state that minimises the free energy $\mathcal{F}$ has many modes, with the magnitudes of all amplitudes equal but with arbitrary phases, then the pattern will resemble a spatially random field (a turbulent crystal). This case will be realised when $B_\theta < 1$ over a wide range of θ [46, 68] (as in figure 8.1, for example). We therefore propose the quasipattern solutions in figure 8.3 (12-, 14- and 20-fold quasipatterns) as examples of turbulent crystals.

It is interesting to consider what determines the number of modes in these turbulent crystals. One argument, explored in more detail by Zhang and Viñals [69], is that

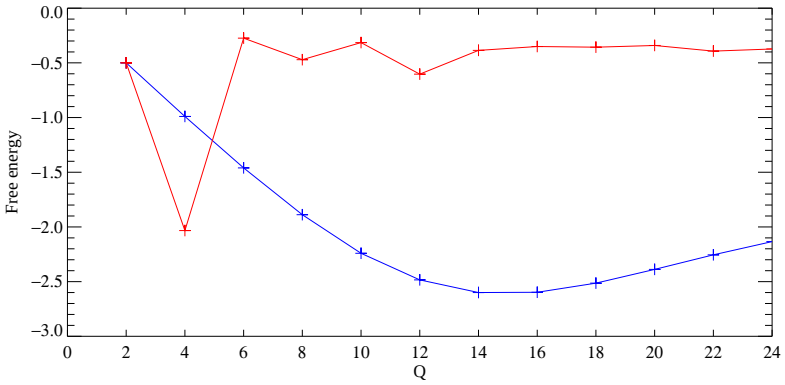

FIG. 8.6. *Value of the free energy $\mathcal{F}$ (8.2) for Q-fold patterns and quasipatterns, derived from the B_θ curves in figure 8.1 with single-frequency forcing (blue) and figure 7.2 with multi-frequency forcing (red).*

the preferred pattern at onset should be the global minimum of the free energy $\mathcal{F}$. Assuming equal amplitudes, the free energy of a Q-fold pattern or quasipattern depends on B_θ evaluated at $360°/Q$, $720°/Q$ *etc.* Figure 8.6 shows $\mathcal{F}$ derived from the B_θ curves in figures 8.1 and 7.2, with single and multi-frequency forcing respectively.

In the single-frequency case (blue curve in figure 8.6), where B_θ is close to zero for $\theta \geq 30°$ (figure 8.1), there is a broad minimum around 14-fold or 16-fold quasipatterns. However, approximate 12-fold, 14-fold, 16-fold and 20-fold examples were found (figure 8.3), depending on the forcing strength and domain size. No doubt other patterns could also be found with more exploration.

In the multi-frequency case (red curve in figure 8.6), where B_θ has pronounced dips at 30° and 90° (figure 7.2), there are local minima at $Q = 4$ (squares), $Q = 8$ and $Q = 12$. In numerical experiments, most initial conditions found squares, though 12-fold quasipatterns were also stable (figures 7.3 and 7.4). We have not looked for 8-fold quasipatterns.

These results suggest that these free energy arguments provide a useful qualitative tool for understanding pattern selection, but reality is often more complicated than the arguments might suggest.

9. Conclusions. We have introduced a new model PDE (3.1) for investigating pattern formation and pattern design in parametrically forced systems. The PDE is intended to play the same role for the Faraday wave experiment that the Swift–Hohenberg equation [61] plays for convection: while the model cannot be derived from the fluid mechanics, it has qualitatively correct linear behaviour and the right type of nonlinear interactions in order to provide useful illumination of the processes that are going on. The model produces superlattice patterns (section 6) and quasipatterns (sections 7 and 8) in response to single and multi-frequency forcing, for the same reasons that these complex patterns are found in the Faraday wave experiment –

confirming that the mechanisms are generic. The ease of calculating weakly nonlinear coefficients and of computing large-scale numerical solutions has allowed a quantitative exploration of the agreement between the theoretical understanding of the pattern selection mechanism and the patterns that are actually found.

Of course, the model does not capture every detail of the physics of the Faraday wave experiment. In particular, the dispersion relations have different structures, and the model does not include the mean flow effects that are important in nearly inviscid Faraday experiments [32]. The latter could be addressed by coupling the model to a conserved quantity or to a mean-flow equation (as in [25,64]) or by taking the negative Laplacian of the right-hand side of the PDE (as in [13, 15]).

The Zhang–Viñals [68] equations do not have these drawbacks: these are derived from the Navier–Stokes equations in the limit of infinite depth and zero viscosity. One might ask what is gained by looking at a simpler PDE that is even further from the physics. There are two advantages of the new model: one is that it is very simple: the dispersion relation can be controlled easily for studying any resonant interaction or response to multi-frequency forcing; in addition, the weakly nonlinear theory can be computed very easily. A second advantage is that is is very well suited to the use of efficient numerical methods such as Exponential Time Differencing [12]: the linear terms are diagonal in Fourier space, and the nonlinear terms do not involve any derivatives. In contrast, the Zhang–Viñals equations are considerably more complicated and the weakly nonlinear computations are more involved. Numerical solutions are also more time-consuming, as the linear term is not diagonal in spectral space, and most of the nonlinear terms involve products of derivatives, resulting in more Fourier transforms for their evaluation. As a result of the relatively low cost of the calculations, we have been able to follow branches of solutions in detail, and to go to much larger domains and for much longer times than previous calculations. Of course, in the end it would be desirable to work directly with the Navier–Stokes equations, but for these, the weakly nonlinear theory is very challenging [58] and there are as yet no large-scale numerical simulations.

Like the Zhang–Viñals equations, the new model includes explicit time dependence. In contrast, other approaches, based on developing a description of the slow evolution of the amplitude of an underlying pattern, use the Ginzburg–Landau equation with additional complex conjugate terms to capture the effect of the time-dependent forcing [8–11, 29]. As a result, any complex patterns that are found must be interpreted in terms of slow, long-wavelength amplitude modulations of an underlying pattern, which complicates any effort to make quantitative comparison between theoretical ideas and the behaviour of the real system. However, within this framework, [9, 10] show that superlattice patterns and quasipatterns are only found if explicit time-dependence is introduced into the Ginzburg–Landau equation by (slowly) modulating the strength of one of the forcing components. The resulting equation is somewhat similar to our model PDE, though the interpretation is different.

The significance of three-wave coupling to weakly damped modes and its role in pattern selection has long been recognised [20, 42, 46, 69]. We have put this idea to a quantitative test by using it to choose forcing functions that stabilise a desired pattern in large domain calculations. However, the codimension-one approach to this idea, where the weakly damped modes are slaved to the pattern-forming modes, does not provide quantitative predictions of amplitudes of patterns, and of parameter regimes where the desired patterns should be stable, except for very close to onset. The reason is that computation of the cross-coupling coefficient B_θ is only valid when all modes are strongly damped compared to the pattern-forming modes. This poses difficulties because the most interesting patterns occur where the pattern-forming modes are coupled to weakly damped modes, and this is where the theory used to calculate properties of these patterns is of limited validity. As a result, parameters had to be chosen very close to onset in order to find stable numerical examples of the desired patterns in parameter regimes where they were predicted to be stable. A codimension-two approach would extend the range of validity of the theory, and will be the subject of future work.

We have investigated two mechanisms for the formation of quasipatterns. One mechanism uses three-wave interactions involving a damped mode associated with the difference of the two frequencies in the forcing to select a particular angle (30° in the example presented here). Using different primary frequencies, or altering the dispersion relation, would allow other angles, or combinations of angles, to be selected. The advantage is that a forcing function can be designed to produce a particular pattern: the mechanism is quite selective, and requires some fine-tuning of the parameters.

The second mechanism uses $1:2$ resonance in space and time to magnify the self-interaction coefficient and thereby, on rescaling, diminish the cross-coupling coefficient B_θ for angles greater than about 30°. This can lead to the formation of turbulent crystals [46]. The mechanism is robust (the patterns are found well above onset), and requires only single frequency forcing. A dispersion relation that supports $1:2$ resonance in space and time is needed. Within this framework, an inherent complication is that it is not clear why regular 8, 10, 12 or 14-fold quasipatterns, or indeed any other combination of modes, should be favoured. Indeed we have found that 12-, 14- and 20-fold approximate quasipatterns can be stabilised by altering the level of the forcing or the domain size, without changing other parameters, and we have reported the transition between two different types of quasipattern. The free energy approach [46, 68] cannot make this distinction, and would predict that 14- or 16-fold quasipatterns should be found at onset for these parameter values (figure 8.6). It remains an open question as to why one turbulent crystal should be favoured over another.

The existence of 14-fold (and higher) quasipatterns has been suggested before [52, 60, 62, 68], but we have presented here the first examples of spontaneously formed 14-fold and 20-fold approximate quasipatterns that are stable solutions of a PDE

(figure 8.3), with preliminary results in [53]. Examples where 14-fold symmetry is imposed externally have been reported in optical experiments [47]. The Fourier spectra of 12-fold and 14-fold quasipatterns are both dense (figure 5.1c,d), but those of 14-fold quasipatterns are much denser, owing to the difference between quadratic and cubic irrational numbers [52]. This difference may have profound consequences for their mathematical treatment.

We have identified what domain sizes result in the most accurate approximations to 12-fold quasipatterns, based on square and on hexagonal domains (table 7.2), and produced exceptionally clean examples of approximate quasipatterns in relatively large computational domains. Comparing the Fourier spectra of the approximate quasipatterns as a function of domain size, we have identified at what order the locations of Fourier modes in the approximate quasipatterns deviate from those of the true quasipatterns. In the largest example (112×112), the locations of the Fourier modes deviate significantly only beyond 26th order (figure 7.6a), at which point the amplitudes of the modes have reached the level of numerical round-off (figure 7.8). This suggests that going any larger than 112×112 would not lead to any significant improvement in the approximation to a true quasipattern, at least for these parameter values.

We have compared the amplitudes of the Fourier modes of the approximate quasipatterns and the leading order weakly nonlinear prediction (figures 7.3 and 8.2), and found quantitative agreement very close to onset, but only qualitative agreement at larger amplitude, which is what would be expected from the problem of eliminating weakly damped modes, as discussed above. We have not extended this comparison to higher order since the weakly nonlinear calculations are too difficult for this parametrically forced problem. An extension of this work would be to devise a PDE without parametric forcing that also produces stable quasipattern solutions. This would allow the use of a larger timestep (since the fast oscillation of the forcing is not present), and so even larger domain numerical computations could be carried out. The lack of parametric forcing would also allow high-order weakly nonlinear calculations (as in [52], where calculations were carried out to 33rd order), and so a quantitative comparison between computed mode amplitudes (as a function of order) and the weakly nonlinear theory would be possible. Standard weakly nonlinear theory produces amplitudes that diverge at high order because of the presence of small divisors [52], while the PDE solutions have amplitudes that appear to decay exponentially with order – although the small divisors in this problem do make themselves felt by amplifying the magnitudes of the Fourier modes at (or close to) the order at which the small divisor appears (figure 7.8). Such a PDE could be based on (for example) the Swift–Hohenberg equation [23, 38, 43], but the Swift–Hohenberg equation itself does not allow the weakly damped modes that are necessary to stabilise quasipatterns.

Other numerical studies of quasipatterns as solutions of a PDE have not made a systematic study of the effect of domain size. Zhang and Viñals [68, 70] report

approximate 8-fold quasipatterns in a 64×64 domain in their quasipotential model of the nearly inviscid Navier–Stokes equations, for parameter values close to the $1:2$ resonance in space and time. The modes involved were separated by 41°, 42°, 48° and 49° [70], so the approximation was not particularly accurate; our careful choice of domain size allowed much closer approximation. Müller [43] developed a model based on two coupled Swift–Hohenberg equations, with parameters chosen so that the two unstable modes had wavenumbers that would favour 8-fold or 12-fold quasipatterns. Numerical simulations in a 10×10 domain in the second case found approximate 12-fold quasipatterns. The modes involved are not stated, but we estimate them to be $\boldsymbol{k}^{(1)} = (10, -1)$, $\boldsymbol{k}^{(2)} = (9, 4)$, $\boldsymbol{k}^{(3)} = (6, 8)$ in units of the fundamental lattice vector. These have lengths 10.05, 9.85 and 10.00 respectively, and they are separated by 28.48° and 29.17°. With $\boldsymbol{k}^{(11)} = (4, -9)$, they have $\boldsymbol{k}^{(3)} + \boldsymbol{k}^{(11)} = \boldsymbol{k}^{(1)}$, so the 60° resonance condition is satisfied. Frisch and Sonnino [23] present a similar model and report 10-fold quasipatterns. Lifshitz and Petrich [38] found a 12-fold approximate quasipattern in a roughly 30×30 domain, in a model based on a single Swift–Hohenberg equation with a degenerate double minimum in its marginal stability curve. The modes involved appear to be the same as those in the 30×30 examples discussed in section 7.

While we have not discussed the possibility of long-wave instabilities of quasipatterns, the Fourier spectra of the 112×112 example (figures 7.6(d) and 7.7) suggests that long-wave modes that are close to the primary wavevectors in a direction *tangent* to the critical circle are forced by high-order nonlinear interactions. This is also apparent from the locations of modes responsible for the small divisors [52]. Therefore, any treatment of the long-wave stability of quasipatterns should take into account the presence of these modes. This is a delicate question. The only study of the sideband instabilities of quasipatterns [19] focusses on instabilities associated with modes that are perpendicular to the unit circle, using coupled Ginzburg–Landau equations for each of the primary mode directions in the quasipattern. This approach could be extended to include instabilities associated with modes that are tangent to the unit circle by looking at coupled Newell–Whitehead–Segel equations, along the lines suggested by [28], although high-order nonlinear interactions may not be captured in a long-wave analysis truncated at cubic order.

Acknowledgments. We are grateful for support from National Science Foundation (DMS-0309667) and from the Engineering and Physical Sciences Research Council (GR/S45928/01). We are also grateful to many people who have helped shape these ideas: Jessica Conway, Stéphan Fauve, Jay Fineberg, Rebecca Hoyle, Gérard Iooss, Edgar Knobloch, Paul Matthews, Ian Melbourne, Werner Pesch, Michael Proctor, Jeff Porter, Hermann Riecke, Anne Skeldon, Jorge Viñals and Gene Wayne. We thank Michael Proctor for pointing out the effect of higher order terms on the centre manifold, discussed in section 6. Finally, we are grateful to the Isaac Newton Institute for Mathematical Sciences, where part of this work was carried out.

REFERENCES

[1] H. Arbell and J. Fineberg, *Two-mode rhomboidal states in driven surface waves*, Phys. Rev. Lett., 84 (2000), pp. 654–657.

[2] ———, *Pattern formation in two-frequency forced parametric waves*, Phys. Rev. E, 65 (2002), p. 036224.

[3] T. B. Benjamin and F. Ursell, *The stability of the plane free surface of a liquid in vertical periodic motion*, Proc. R. Soc. Lond. A, 225 (1954), pp. 505–515.

[4] T. Besson, W. S. Edwards, and L. S. Tuckerman, *Two-frequency parametric excitation of surface waves*, Phys. Rev. E, 54 (1996), pp. 507–513.

[5] D. Binks and W. van de Water, *Nonlinear pattern formation of Faraday waves*, Phys. Rev. Lett., 78 (1997), pp. 4043–4046.

[6] D. Binks, M. T. Westra, and W. van de Water, *Effect of depth on the pattern formation of Faraday waves*, Phys. Rev. Lett., 79 (1997), pp. 5010–5013.

[7] B. Christiansen, P. Alstrom, and M. T. Levinsen, *Ordered capillary-wave states: Quasicrystals, hexagons, and radial waves*, Phys. Rev. Lett., 68 (1992), pp. 2157–2160.

[8] J. M. Conway and H. Riecke, *Multiresonant forcing of the complex Ginzburg–Landau equation: Pattern selection*, Phys. Rev. E, 76 (2007), p. 057202.

[9] ———, *Quasipatterns in a model for chemical oscillations forced at multiple resonance frequencies*, Phys. Rev. Lett., 99 (2007), p. 218301.

[10] ———, *Superlattice patterns in the complex Ginzburg–Landau equation with multi-resonant forcing*. 2008.

[11] P. Coullet and K. Emilsson, *Strong resonances of spatially distributed oscillators: a laboratory to study patterns and defects*, Physica D, 61 (1992), pp. 119–131.

[12] S. M. Cox and P. C. Matthews, *Exponential time differencing for stiff systems*, J. Comp. Phys., 176 (2002), pp. 430–455.

[13] ———, *Instability and localisation of patterns due to a conserved quantity*, Physica D, 175 (2003), pp. 196–219.

[14] M. C. Cross and P. C. Hohenberg, *Pattern formation outside of equilibrium*, Rev. Mod. Phys., 65 (1993), pp. 851–1112.

[15] J. H. P. Dawes, P. C. Matthews, and A. M. Rucklidge, *Reducible actions of $D_4 \ltimes T^2$: superlattice patterns and hidden symmetries*, Nonlinearity, 16 (2003), pp. 615–645.

[16] G. Dewel, M. Bachir, P. Borckmans, and S. Metens, *Superlattice structures and quasipatterns in bistable systems*, C. R. Acad. Sci. Ser. IIb, 329 (2001), pp. 411–416.

[17] Y. Ding and P. Umbanhowar, *Enhanced Faraday pattern stability with three-frequency driving*, Phys. Rev. E, 73 (2006), p. 046305.

[18] B. Dionne, M. Silber, and A. C. Skeldon, *Stability results for steady, spatially periodic planforms*, Nonlinearity, 10 (1997), pp. 321–353.

[19] B. Echebarria and H. Riecke, *Sideband instabilities and defects of quasipatterns*, Physica D, 158 (2001), pp. 45–68.

[20] W. S. Edwards and S. Fauve, *Patterns and quasi-patterns in the Faraday experiment*, J. Fluid Mech., 278 (1994), pp. 123–148.

[21] T. Epstein and J. Fineberg, *Grid states and nonlinear selection in parametrically excited surface waves*, Phys. Rev. E, 73 (2006), p. 055302(R).

[22] M. Frigo and S. G. Johnson, *The design and implementation of FFTW3*, Proc. IEEE, 93 (2005), pp. 216–231.

[23] T. Frisch and G. Sonnino, *2-dimensional pentagonal structures in dissipative systems*, Phys. Rev. E, 51 (1995), pp. 1169–1171.

[24] M. Golubitsky, I. Stewart, and D. G. Schaeffer, *Singularities and Groups in Bifurcation Theory. Volume II*, Springer, New York, 1988.

[25] H. S. Greenside and M. C. Cross, *Stability analysis of two-dimensional models of 3-dimensional convection*, Phys. Rev. A, 31 (1985), pp. 2492–2501.

[26] P. G. Grinevich and P. M. Santini, *Newtonian dynamics in the plane corresponding to straight and cyclic motions on the hyperelliptic curve $\mu^2 = \nu^n - 1$, $n \in \mathbb{Z}$: Ergodicity, isochrony and fractals*, Physica D, 232 (2007), pp. 22–32.

[27] J. Guckenheimer and P. Holmes, *Nonlinear Oscillations, Dynamical Systems and Bifurcations of Vector Fields*, Springer, New York, 1983.

[28] G. H. Gunaratne, Q. Ouyang, and H. L. Swinney, *Pattern formation in the presence of symmetries*, Phys. Rev. E, 50 (1994), pp. 2802–2820.

[29] J. Halloy, G. Sonnino, and P. Coullet, *Pattern formation in forced reaction diffusion systems with nearly degenerate bifurcations*, Chaos, 17 (2007), p. 037107.

[30] R. Herrero, E. G. Westhoff, A. Aumann, T. Ackemann, Y. A. Logvin, and W. Lange, *Twelvefold quasiperiodic patterns in a nonlinear optical system with continuous rotational symmetry*, Phys. Rev. Lett., 82 (1999), pp. 4627–4630.

[31] R. B. Hoyle, *Pattern Formation: an Introduction to Methods*, Cambridge University Press, Cambridge, 2006.

[32] E. Knobloch, C. Martel, and J. M. Vega, *Coupled mean flow-amplitude equations for nearly inviscid parametrically driven surface waves*, Ann. N. Y. Acad. Sci., 974 (2002), pp. 201–219.

[33] A. Kudrolli and J. P. Gollub, *Patterns and spatiotemporal chaos in parametrically forced surface waves: A systematic survey at large aspect ratio*, Physica D, 97 (1996), pp. 133–154.

[34] A. Kudrolli, B. Pier, and J. P. Gollub, *Superlattice patterns in surface waves*, Physica D, 123 (1998), pp. 99–111.

[35] K. Kumar, *Linear theory of Faraday instability in viscous liquids*, Proc. R. Soc. Lond. A, 452 (1996), pp. 1113–1126.

[36] K. Kumar and L. S. Tuckerman, *Parametric instability of the interface between 2 fluids*, J. Fluid Mech., 279 (1994), pp. 49–68.

[37] R. Lifshitz and H. Diamant, *Soft quasicrystals: Why are they stable?*, Philos. Mag., 87 (2007), pp. 3021–3030.

[38] R. Lifshitz and D. M. Petrich, *Theoretical model for Faraday waves with multiple-frequency forcing*, Phys. Rev. Lett., 79 (1997), pp. 1261–1264.

[39] P. C. Matthews, *Hexagonal patterns in finite domains*, Physica D, 116 (1998), pp. 81–94.

[40] P. C. Matthews and S. M. Cox, *Pattern formation with a conservation law*, Nonlinearity, 13 (2000), pp. 1293–1320.

[41] I. Melbourne, *Derivation of the time-dependent Ginzburg–Landau equation on the line*, J. Nonlin. Sci., 8 (1998), pp. 1–15.

[42] N. D. Mermin and S. M. Troian, *Mean-field theory of quasicrystalline order*, Phys. Rev. Lett., 54 (1985), pp. 1524–1527.

[43] H. W. Muller, *Model-equations for 2-dimensional quasipatterns*, Phys. Rev. E, 49 (1994), pp. 1273–1277.

[44] H. W. Muller, R. Friedrich, and D. Papathanassiou, *Theoretical and experimental investigations of the Faraday instability*, in Evolution of Spontaneous Structures in Dissipative Continuous Systems, F. H. Busse and S. C. Müller, eds., Springer, Berlin, 1998, pp. 230–265.

[45] H. W. Muller, H. Wittmer, C. Wagner, J. Albers, and K. Knorr, *Analytic stability theory for Faraday waves and the observation of the harmonic surface response*, Phys. Rev. Lett., 78 (1997), pp. 2357–2360.

[46] A. C. Newell and Y. Pomeau, *Turbulent crystals in macroscopic systems*, J. Phys. A, 26 (1993), pp. L429–L434.

[47] E. Pampaloni, P. L. Ramazza, S. Residori, and F. T. Arecchi, *2-dimensional crystals and quasi-crystals in nonlinear optics*, Phys. Rev. Lett., 74 (1995), pp. 258–261.

[48] J. Porter and M. Silber, *Broken symmetries and pattern formation in two-frequency forced Faraday waves*, Phys. Rev. Lett., 89 (2002), p. 084501.

[49] ———, *Resonant triad dynamics in weakly damped Faraday waves with two-frequency forcing*,

Physica D, 190 (2004), pp. 93–114.

[50] J. Porter, C. M. Topaz, and M. Silber, *Pattern control via multifrequency parametric forcing*, Phys. Rev. Lett., 93 (2004), p. 034502.

[51] J. L. Rogers, W. Pesch, O. Brausch, and M. F. Schatz, *Complex-ordered patterns in shaken convection*, Phys. Rev. E, 71 (2005), p. 066214.

[52] A. M. Rucklidge and W. J. Rucklidge, *Convergence properties of the 8, 10 and 12 mode representations of quasipatterns*, Physica D, 178 (2003), pp. 62–82.

[53] A. M. Rucklidge and M. Silber, *Quasipatterns in parametrically forced systems*, Phys. Rev. E, 75 (2007), p. 055203.

[54] D. Shechtman, I. Blech, D. Gratias, and J. W. Cahn, *Metallic phase with long-range orientational order and no translational symmetry*, Phys. Rev. Lett., 53 (1984), pp. 1951–1953.

[55] M. Silber and M. R. E. Proctor, *Nonlinear competition between small and large hexagonal patterns*, Phys. Rev. Lett., 81 (1998), pp. 2450–2453.

[56] M. Silber and A. C. Skeldon, *Parametrically excited surface waves: Two-frequency forcing, normal form symmetries, and pattern selection*, Phys. Rev. E, 59 (1999), pp. 5446–5456.

[57] M. Silber, C. M. Topaz, and A. C. Skeldon, *Two-frequency forced Faraday waves: weakly damped modes and pattern selection*, Physica D, 143 (2000), pp. 205–225.

[58] A. C. Skeldon and G. Guidoboni, *Pattern selection for Faraday waves in an incompressible viscous fluid*, SIAM J. Appl. Math., 67 (2007), pp. 1064–1100.

[59] H. G. Solari and G. B. Mindlin, *Quasicrystals and strong interactions between square modes*, Phys. Rev. E, 56 (1997), pp. 1853–1858.

[60] W. Steurer, *Boron-based quasicrystals with sevenfold symmetry*, Philos. Mag., 87 (2007), pp. 2707–2712.

[61] J. Swift and P. C. Hohenberg, *Hydrodynamic fluctuations at the convective instability*, Phys. Rev. A, 15 (1977), pp. 319–328.

[62] C. M. Topaz, J. Porter, and M. Silber, *Multifrequency control of Faraday wave patterns*, Phys. Rev. E, 70 (2004), p. 066206.

[63] C. M. Topaz and M. Silber, *Resonances and superlattice pattern stabilization in two-frequency forced Faraday waves*, Physica D, 172 (2002), pp. 1–29.

[64] L. S. Tsimring and I. S. Aranson, *Localized and cellular patterns in a vibrated granular layer*, Phys. Rev. Lett., 79 (1997), pp. 213–216.

[65] U. E. Volmar and H. W. Muller, *Quasiperiodic patterns in Rayleigh–Bénard convection under gravity modulation*, Phys. Rev. E, 56 (1997), pp. 5423–5430.

[66] C. Wagner, H. W. Muller, and K. Knorr, *Pattern formation at the bicritical point of the Faraday instability*, Phys. Rev. E, 68 (2003), p. 066204.

[67] M. T. Westra, D. J. Binks, and W. Van de Water, *Patterns of Faraday waves*, J. Fluid Mech., 496 (2003), pp. 1–32.

[68] W. B. Zhang and J. Viñals, *Square patterns and quasipatterns in weakly damped Faraday waves*, Phys. Rev. E, 53 (1996), pp. R4283–R4286.

[69] ———, *Pattern formation in weakly damped parametric surface waves*, J. Fluid Mech., 336 (1997), pp. 301–330.

[70] ———, *Numerical study of pattern formation in weakly damped parametric surface waves*, Physica D, 116 (1998), pp. 225–243.

Appendix A. Linear and weakly nonlinear theory.

In this appendix, we present the linear and weakly nonlinear theory for the PDE (3.1). We will describe the calculation in terms of a harmonic primary bifurcation; the subharmonic case is similar, with the main differences being that the period is 4π rather then 2π, and that the quadratic coefficient Q is identically zero.

We start by writing $U = u + iv$, where $u(x, y, t)$ and $v(x, y, t)$ are real functions,

and so

$$\begin{aligned}\frac{\partial u}{\partial t} &= \left(\mu+\alpha\nabla^2+\gamma\nabla^4\right)u - \left(\omega+\beta\nabla^2+\delta\nabla^4\right)v \\ &\quad + Q_{1r}(u^2-v^2) - Q_{1i}(2uv) + Q_{2r}(u^2+v^2) + C_r(u^2+v^2)u - C_i(u^2+v^2)v \\ \frac{\partial v}{\partial t} &= \left(\omega+\beta\nabla^2+\delta\nabla^4\right)u + \left(\mu+\alpha\nabla^2+\gamma\nabla^4\right)v \\ &\quad + Q_{1i}(u^2-v^2) + Q_{1r}(2uv) + Q_{2i}(u^2+v^2) + C_r(u^2+v^2)v + C_i(u^2+v^2)u \\ &\quad + f(t)u.\end{aligned}$$

We define differential operators $\mathcal{L}$ and $\mathcal{M}$:

$$\mathcal{L} = \frac{\partial}{\partial t} - \left(\mu+\alpha\nabla^2+\gamma\nabla^4\right) \qquad \text{and} \qquad \mathcal{M} = \left(\omega+\beta\nabla^2+\delta\nabla^4\right),$$

so the PDEs for u and v are

$$\begin{aligned}\mathcal{L}u &= -\mathcal{M}v + \mathrm{NL}_u, \\ \mathcal{L}v &= \quad \mathcal{M}u + \mathrm{NL}_v + f(t)u.\end{aligned}$$

The nonlinear terms NL_u and NL_v are:

$$\begin{aligned}\mathrm{NL}_u &= Q_{1r}(u^2-v^2) - Q_{1i}(2uv) + Q_{2r}(u^2+v^2) + C_r(u^2+v^2)u - C_i(u^2+v^2)v, \\ \mathrm{NL}_v &= Q_{1i}(u^2-v^2) + Q_{1r}(2uv) + Q_{2i}(u^2+v^2) + C_r(u^2+v^2)v + C_i(u^2+v^2)u.\end{aligned}$$

A.1. Linear theory. We seek solutions of the form $u = e^{i\boldsymbol{k}\cdot\boldsymbol{x}}p_1(t)$ and $v = e^{i\boldsymbol{k}\cdot\boldsymbol{x}}q_1(t)$, where p_1 and q_1 are periodic functions of period T, and defining

$$\hat{\gamma}_1 = 2\left(-\mu+\alpha k^2-\gamma k^4\right), \qquad \hat{\Omega}_1 = \omega-\beta k^2+\delta k^4, \qquad \Omega_1 = \sqrt{\left(\frac{\hat{\gamma}_1}{2}\right)^2 + \left(\hat{\Omega}_1\right)^2},$$

we get the linearised equations

$$\begin{aligned}\mathcal{L}_1 p_1 &= -\mathcal{M}_1 q_1, \\ \mathcal{L}_1 q_1 &= \quad \mathcal{M}_1 p_1 + f(t)p_1,\end{aligned}$$

or

$$\mathcal{L}_1^2 p_1 = -\mathcal{M}_1\mathcal{L}_1 q_1 = -\mathcal{M}_1^2 p_1 - f(t)\mathcal{M}_1 p_1,$$

where $\mathcal{L}_1$ and $\mathcal{M}_1$ act on $p_1(t)$ and $q_1(t)$ as

$$\mathcal{L}_1 = \frac{d}{dt} + \frac{\hat{\gamma}_1}{2} \qquad \text{and} \qquad \mathcal{M}_1 = \hat{\Omega}_1.$$

The linearised PDE thus reduces to a damped Mathieu equation for p_1:

$$\left(\frac{d}{dt}+\frac{\hat{\gamma}_1}{2}\right)^2 p_1 + \hat{\Omega}_1^2 p_1 + f(t)\hat{\Omega}_1 p_1 = 0$$

or (defining a linear operator $\mathbf{L}$):

$$\ddot{p}_1 + \hat{\gamma}_1\dot{p}_1 + \left(\Omega_1^2 + \hat{\Omega}_1 f(t)\right) p_1 = 0 = \mathbf{L}p_1.$$

The adjoint equation is:

$$\ddot{\tilde{p}}_1 - \hat{\gamma}_1\dot{\tilde{p}}_1 + \left(\Omega_1^2 + \hat{\Omega}_1 f(t)\right) \tilde{p}_1 = 0 = \tilde{\mathbf{L}}\tilde{p}_1,$$

defined with respect to an inner product

$$\langle g, h\rangle = \frac{1}{T}\int_0^T g(t)h(t)\,dt,$$

with $T = 2\pi$ (harmonic case) or $T = 4\pi$ (subharmonic case), so $\langle g, \mathbf{L}h\rangle = \langle \tilde{\mathbf{L}}g, h\rangle$ for T-periodic functions g and h.

For a given value of k, seeking non-zero periodic solutions of $\mathbf{L}p = 0$ yields an eigenvalue problem whose eigenvalue is the amplitude of the forcing function $f(t)$. We use the method of [4] to solve this eigenvalue problem with multi-frequency forcing $f(t)$, providing the critical forcing amplitude. Minimising this critical forcing amplitude over k yields the critical wavenumber k_c, critical forcing function $f_c(t)$, and critical eigenfunction $p_1(t)$. The corresponding $q_1(t)$ is determined by solving $\mathcal{L}_1 q_1 = \hat{\Omega}p_1 + f_c(t)p_1$.

A.2. Rhombs. We consider f close to f_c, writing $f(t) = f_c(t)(1 + \epsilon^2 F_2)$, and seek small-amplitude rhombic solutions associated with two wavevectors $\boldsymbol{k}_1$ and $\boldsymbol{k}_2$ at the critical wavenumber: $|\boldsymbol{k}_1| = |\boldsymbol{k}_2| = k_c$, separated by an angle θ. (For ease of notation, in this Appendix, we use subscripts to index wavevectors and suppress explicit reference to the forcing frequency.) We formally expand the solution as

$$\begin{aligned}
u &= \epsilon u_1 + \epsilon^2 u_2 + \epsilon^3 u_3 + \cdots \\
&= \epsilon\left(z_1(T_2)e^{i\boldsymbol{k}_1\cdot\boldsymbol{x}} + z_2(T_2)e^{i\boldsymbol{k}_2\cdot\boldsymbol{x}} + c.c.\right)p_1(t) \\
&\quad + \epsilon^2\Big(\left(z_1^2 e^{2i\boldsymbol{k}_1\cdot\boldsymbol{x}} + z_2^2 e^{2i\boldsymbol{k}_2\cdot\boldsymbol{x}} + c.c.\right)p_2(t) + \left(|z_1|^2 + |z_2|^2\right)p_3(t) \\
&\qquad + \left(z_1 z_2 e^{i(\boldsymbol{k}_1+\boldsymbol{k}_2)\cdot\boldsymbol{x}} + c.c.\right)p_4(t) + \left(z_1\bar{z}_2 e^{i(\boldsymbol{k}_1-\boldsymbol{k}_2)\cdot\boldsymbol{x}} + c.c.\right)p_5(t)\Big) + \mathcal{O}(\epsilon^3),
\end{aligned}$$

with a similar expression for v in terms of v_1, v_2 and v_3, and q_1, ..., q_5, where T_2 is a slow time, varying on a scale of ϵ^{-2}, and the functions $p_2(t)$, ..., $q_5(t)$ are to be determined. The form of this solution is chosen by knowing in advance the structure of the nonlinear terms and the modes to be generated by them.

Substituting these expressions for u and v into the PDE and ordering in powers of ϵ, we recover, at leading order in ϵ, the linear theory. At second order in ϵ, we split the PDE into terms that go as $e^{2i\boldsymbol{k}_1\cdot\boldsymbol{x}}$, $e^{2i\boldsymbol{k}_2\cdot\boldsymbol{x}}$, terms without spatial dependence, and terms that go as $e^{i(\boldsymbol{k}_1+\boldsymbol{k}_2)\cdot\boldsymbol{x}}$ and $e^{i(\boldsymbol{k}_1-\boldsymbol{k}_2)\cdot\boldsymbol{x}}$.

The terms like $e^{2i\boldsymbol{k}_1\cdot\boldsymbol{x}}$ lead to equations for p_2 and q_2:

$$\begin{aligned}
\mathcal{L}_2 p_2 &= -\mathcal{M}_2 q_2 + \mathrm{NL}_{p2}^{(2)}, \\
\mathcal{L}_2 q_2 &= \quad \mathcal{M}_2 p_2 + \mathrm{NL}_{q2}^{(2)} + f_c(t)p_2,
\end{aligned}$$

where the linear operators are:

$$\mathcal{L}_2 = \frac{d}{dt} - \left(\mu - 4\alpha k_c^2 + 16\gamma k_c^4\right) = \frac{d}{dt} + \frac{\hat{\gamma}_2}{2},$$
$$\mathcal{M}_2 = \left(\omega - 4\beta k_c^2 + 16\delta k_c^4\right) = \hat{\Omega}_2,$$

and the nonlinear terms $\mathrm{NL}_{p2}^{(2)}$ and $\mathrm{NL}_{q2}^{(2)}$ are:

$$\mathrm{NL}_{p2}^{(2)} = Q_{1r}(p_1^2 - q_1^2) - Q_{1i}(2p_1q_1) + Q_{2r}(p_1^2 + q_1^2),$$
$$\mathrm{NL}_{q2}^{(2)} = Q_{1i}(p_1^2 - q_1^2) + Q_{1r}(2p_1q_1) + Q_{2i}(p_1^2 + q_1^2).$$

The function q_2 is eliminated by operating with $\mathcal{L}_2$, resulting in a second-order non-constant coefficient inhomogeneous linear ODE for p_2:

$$\left(\mathcal{L}_2^2 + \mathcal{M}_2^2 + \mathcal{M}_2 f(t)\right) p_2 = \mathcal{L}_2 \mathrm{NL}_{p2}^{(2)} - \mathcal{M}_2 \mathrm{NL}_{q2}^{(2)}.$$

or

$$\ddot{p}_2 + \hat{\gamma}_2 \dot{p}_2 + \left(\Omega_2^2 + \hat{\Omega}_2 f_c(t)\right) p_2 = \left(\frac{d}{dt} + \frac{\hat{\gamma}_2}{2}\right) \mathrm{NL}_{p2}^{(2)} - \hat{\Omega}_2 \mathrm{NL}_{q2}^{(2)}.$$

This can be solved numerically for p_2 using Fourier transform methods, and q_2 can then be found. Terms that go as $e^{2i\boldsymbol{k}_2\cdot\boldsymbol{x}}$ result in the same equation.

Terms without spatial dependence, and terms with spatial dependence $e^{i(\boldsymbol{k}_1+\boldsymbol{k}_2)\cdot\boldsymbol{x}}$ and $e^{i(\boldsymbol{k}_1-\boldsymbol{k}_2)\cdot\boldsymbol{x}}$, result in similar equations for p_3, p_4 and p_5, but with linear operators:

$$\mathcal{L}_3 = \frac{d}{dt} - \mu = \frac{d}{dt} + \frac{\hat{\gamma}_3}{2}, \qquad \text{and} \qquad \mathcal{M}_3 = \omega = \hat{\Omega}_3,$$
$$\mathcal{L}_4 = \frac{d}{dt} - \left(\mu - 4\cos^2\left(\frac{\theta}{2}\right)\alpha k_c^2 + 16\cos^4\left(\frac{\theta}{2}\right)\gamma k_c^4\right) = \frac{d}{dt} + \frac{\hat{\gamma}_4}{2},$$
$$\mathcal{M}_4 = \left(\omega - 4\cos^2\left(\frac{\theta}{2}\right)\beta k_c^2 + 16\cos^4\left(\frac{\theta}{2}\right)\delta k_c^4\right) = \hat{\Omega}_4,$$
$$\mathcal{L}_5 = \frac{d}{dt} - \left(\mu - 4\sin^2\left(\frac{\theta}{2}\right)\alpha k_c^2 + 16\sin^4\left(\frac{\theta}{2}\right)\gamma k_c^4\right) = \frac{d}{dt} + \frac{\hat{\gamma}_5}{2},$$
$$\mathcal{M}_5 = \left(\omega - 4\sin^2\left(\frac{\theta}{2}\right)\beta k_c^2 + 16\sin^4\left(\frac{\theta}{2}\right)\delta k_c^4\right) = \hat{\Omega}_5,$$

and nonlinear terms:

$$\mathrm{NL}_{p3}^{(2)} = \mathrm{NL}_{p4}^{(2)} = \mathrm{NL}_{p5}^{(2)} = 2\mathrm{NL}_{p2}^{(2)},$$
$$\mathrm{NL}_{q3}^{(2)} = \mathrm{NL}_{q4}^{(2)} = \mathrm{NL}_{q5}^{(2)} = 2\mathrm{NL}_{q2}^{(2)}.$$

Note that $\hat{\gamma}_4$, $\hat{\gamma}_5$, $\hat{\Omega}_4$ and $\hat{\Omega}_5$ depend on θ, the angle between the chosen wavevectors, whereas $\hat{\gamma}_1$, $\hat{\gamma}_2$, $\hat{\gamma}_3$, $\hat{\Omega}_1$, $\hat{\Omega}_2$ and $\hat{\Omega}_3$ do not.

At third order in ϵ, the problem has the following structure:

$$\mathcal{L}u_3 + \frac{\partial u_1}{\partial T_2} = -\mathcal{M}v_3 + \mathrm{NL}_u^{(3)},$$
$$\mathcal{L}v_3 + \frac{\partial v_1}{\partial T_2} = \quad \mathcal{M}u_3 + \mathrm{NL}_v^{(3)} + f_c(t)u_3 + F_2 f_c(t)u_1.$$

The nonlinear terms $\mathrm{NL}_u^{(3)}$ and $\mathrm{NL}_v^{(3)}$ are:

$$\begin{aligned}\mathrm{NL}_u^{(3)} &= 2Q_{1r}(u_1u_2 - v_1v_2) - Q_{1i}(2u_1v_2 + 2u_2v_1) + 2Q_{2r}(u_1u_2 + v_1v_2)\\ &\quad + C_r(u_1^2 + v_1^2)u_1 - C_i(u_1^2 + v_1^2)v_1,\\ \mathrm{NL}_v^{(3)} &= 2Q_{1i}(u_1u_2 - v_1v_2) + Q_{1r}(2u_1v_2 + 2u_2v_1) + 2Q_{2i}(u_1u_2 + v_1v_2)\\ &\quad + C_r(u_1^2 + v_1^2)v_1 + C_i(u_1^2 + v_1^2)u_1.\end{aligned}$$

Eliminating v_3, we obtain

$$\left(\mathcal{L}^2 + \mathcal{M}^2 + \mathcal{M}f_c\right)u_3 = -\mathcal{L}\frac{\partial u_1}{\partial T_2} + \mathcal{M}\frac{\partial v_1}{\partial T_2} - \mathcal{M}F_2f_cu_1 + \mathcal{L}\mathrm{NL}_u^{(3)} - \mathcal{M}\mathrm{NL}_v^{(3)}.$$

The operator on the left is the singular operator $\mathbf{L}$ from the linearised problem, so the equation can only be solved for u_3 if a solvability condition is applied to the terms that are proportional to $e^{i\boldsymbol{k}_1\cdot\boldsymbol{x}}$ and $e^{i\boldsymbol{k}_2\cdot\boldsymbol{x}}$ and complex conjugates. If we take the inner product between $\tilde{p}_1$ and the $e^{i\boldsymbol{k}_1\cdot\boldsymbol{x}}$ component of the above, we find

$$\tau\frac{\partial z_1}{\partial T_2} = \sigma F_2 z_1 + \left(\hat{A}|z_1|^2 + (\hat{B}_{\mathrm{indep}} + \hat{B}_{\mathrm{res}}(\theta))|z_2|^2\right)z_1,$$

with a similar equation for z_2, where

$$\tau = \left\langle \tilde{p}_1, 2\left(\dot{p}_1 + \frac{\hat{\gamma}_1}{2}p_1\right)\right\rangle \qquad \text{and} \qquad \sigma = \left\langle \tilde{p}_1, -\hat{\Omega}_1 f_c p_1\right\rangle$$

(using $\mathcal{L}_1 p_1 = -\mathcal{M}_1 q_1$) and

$$\begin{aligned}
\hat{A} = \Big\langle \tilde{p}_1, \Big(\frac{d}{dt} + \frac{\hat{\gamma}_1}{2}\Big)\Big(&2Q_{1r}(p_1p_2 + p_1p_3 - q_1q_2 - q_1q_3) \\
&- 2Q_{1i}(p_1q_2 + p_1q_3 + q_1p_2 + q_1p_3) \\
&+ 2Q_{2r}(p_1p_2 + p_1p_3 + q_1q_2 + q_1q_3) \\
&+ 3C_r(p_1^2 + q_1^2)p_1 - 3C_i(p_1^2 + q_1^2)q_1\Big) \\
- \hat{\Omega}_1\Big(&2Q_{1r}(p_1q_2 + p_1q_3 + q_1p_2 + q_1p_3) \\
&+ 2Q_{1i}(p_1p_2 + p_1p_3 - q_1q_2 - q_1q_3) \\
&+ 2Q_{2i}(p_1p_2 + p_1p_3 + q_1q_2 + q_1q_3) \\
&+ 3C_r(p_1^2 + q_1^2)q_1 + 3C_i(p_1^2 + q_1^2)p_1\Big)\Big\rangle, \\
\hat{B}_{\text{indep}} = \Big\langle \tilde{p}_1, \Big(\frac{d}{dt} + \frac{\hat{\gamma}_1}{2}\Big)\Big(&2Q_{1r}(p_1p_3 - q_1q_3) - 2Q_{1i}(p_1q_3 + q_1p_3) \\
&+ 2Q_{2r}(p_1p_3 + q_1q_3) + 6C_r(p_1^2 + q_1^2)p_1 - 6C_i(p_1^2 + q_1^2)q_1\Big) \\
- \hat{\Omega}_1\Big(&2Q_{1r}(p_1q_3 + q_1p_3) + 2Q_{1i}(p_1p_3 - q_1q_3) + 2Q_{2i}(p_1p_3 + q_1q_3) \\
&+ 6C_r(p_1^2 + q_1^2)q_1 + 6C_i(p_1^2 + q_1^2)p_1\Big)\Big\rangle, \\
\hat{B}_{\text{res}}(\theta) = \Big\langle \tilde{p}_1, \Big(\frac{d}{dt} + \frac{\hat{\gamma}_1}{2}\Big)\Big(&2Q_{1r}(p_1p_4 + p_1p_5 - q_1q_4 - q_1q_5) \\
&- 2Q_{1i}(p_1q_4 + p_1q_5 + q_1p_4 + q_1p_5) \\
&+ 2Q_{2r}(p_1p_4 + p_1p_5 + q_1q_4 + q_1q_5)\Big) \\
- \hat{\Omega}_1\Big(&2Q_{1r}(p_1q_4 + p_1q_5 + q_1p_4 + q_1p_5) \\
&+ 2Q_{1i}(p_1p_4 + p_1p_5 - q_1q_4 - q_1q_5) \\
&+ 2Q_{2i}(p_1p_4 + p_1p_5 + q_1q_4 + q_1q_5)\Big)\Big\rangle.
\end{aligned}$$

For convenience, we have separated the parts of the cross-coupling coefficient that do not depend on the angle between the modes ($\hat{B}_{\text{indep}}$) from those that do ($\hat{B}_{\text{res}}(\theta)$). We discuss below how these coefficients are then scaled.

A.3. Hexagons. As with rhombs, we look for f close to f_c, writing $f(t) = f_c(t)(1+\epsilon^2 F_2)$, but now we choose three wavevectors, $\boldsymbol{k}_1$, $\boldsymbol{k}_2$ and $\boldsymbol{k}_3$ oriented at 120° to each other, with $\boldsymbol{k}_1 + \boldsymbol{k}_2 + \boldsymbol{k}_3 = \boldsymbol{0}$. We look for small-amplitude solutions with

equal amplitudes of the three waves, and write

$$\begin{aligned}u &= \epsilon u_1 + \epsilon^2 u_2 + \epsilon^3 u_3 + \cdots \\ &= \epsilon z(T_1,T_2)\left(e^{i\boldsymbol{k}_1\cdot\boldsymbol{x}} + e^{i\boldsymbol{k}_2\cdot\boldsymbol{x}} + e^{i\boldsymbol{k}_3\cdot\boldsymbol{x}} + c.c.\right)p_1(t) \\ &\quad + \epsilon^2\Big(z^2\left(e^{2i\boldsymbol{k}_1\cdot\boldsymbol{x}} + e^{2i\boldsymbol{k}_2\cdot\boldsymbol{x}} + e^{2i\boldsymbol{k}_3\cdot\boldsymbol{x}} + c.c.\right)p_2(t) + 3|z|^2 p_3(t) \\ &\qquad + |z|^2\left(e^{i(\boldsymbol{k}_1-\boldsymbol{k}_2)\cdot\boldsymbol{x}} + e^{i(\boldsymbol{k}_2-\boldsymbol{k}_3)\cdot\boldsymbol{x}} + e^{i(\boldsymbol{k}_3-\boldsymbol{k}_1)\cdot\boldsymbol{x}} + c.c.\right)\tilde{p}_5(t) \\ &\qquad + \bar{z}^2\left(e^{i\boldsymbol{k}_1\cdot\boldsymbol{x}} + e^{i\boldsymbol{k}_2\cdot\boldsymbol{x}} + e^{i\boldsymbol{k}_3\cdot\boldsymbol{x}} + c.c.\right)p_6(t)\Big) + \mathcal{O}(\epsilon^3),\end{aligned}$$

with a similar expression for v in terms of q_1, ..., q_6, where T_1 and T_2 are slow times, varying on scales ϵ^{-1} and ϵ^{-2}, and the functions $p_2(t)$, ..., $q_6(t)$ are to be determined. The form of the expression is chosen by knowing in advance the structure of the nonlinear terms.

Substituting these expressions for u and v into the PDE and ordering in powers of ϵ, at leading order in ϵ we recover the linear theory. At second order in ϵ, we split the PDE into terms that go as $e^{2i\boldsymbol{k}_1\cdot\boldsymbol{x}} + e^{2i\boldsymbol{k}_2\cdot\boldsymbol{x}} + e^{2i\boldsymbol{k}_3\cdot\boldsymbol{x}} + c.c.$, terms without spatial dependence, terms that go as $e^{i(\boldsymbol{k}_1-\boldsymbol{k}_2)\cdot\boldsymbol{x}} + e^{i(\boldsymbol{k}_2-\boldsymbol{k}_3)\cdot\boldsymbol{x}} + e^{i(\boldsymbol{k}_3-\boldsymbol{k}_1)\cdot\boldsymbol{x}} + c.c.$, and finally terms that go as $e^{i\boldsymbol{k}_1\cdot\boldsymbol{x}} + e^{i\boldsymbol{k}_2\cdot\boldsymbol{x}} + e^{i\boldsymbol{k}_3\cdot\boldsymbol{x}} + c.c.$, which have to be considered specially.

Terms like $e^{2i\boldsymbol{k}_1\cdot\boldsymbol{x}} + e^{2i\boldsymbol{k}_2\cdot\boldsymbol{x}} + e^{2i\boldsymbol{k}_3\cdot\boldsymbol{x}} + c.c.$ and terms without spatial dependence give the same equations for p_2, q_2, p_3 and q_3 as in the case of rhombs. In particular, the inhomogeneous nonlinear terms are the same. Terms that go as $e^{i(\boldsymbol{k}_1-\boldsymbol{k}_2)\cdot\boldsymbol{x}} + e^{i(\boldsymbol{k}_2-\boldsymbol{k}_3)\cdot\boldsymbol{x}} + e^{i(\boldsymbol{k}_3-\boldsymbol{k}_1)\cdot\boldsymbol{x}} + c.c.$ result in equations for $\tilde{p}_5$ and $\tilde{q}_5$ that are the equations for p_5 and q_5 evaluated for $\theta = 120°$.

Terms that go as $e^{i\boldsymbol{k}_1\cdot\boldsymbol{x}} + e^{i\boldsymbol{k}_2\cdot\boldsymbol{x}} + e^{i\boldsymbol{k}_3\cdot\boldsymbol{x}} + c.c.$ require the use of two time-scales and a solvability condition. The linear operators are the same as for the initial linear problem:

$$\begin{aligned}\mathcal{L}_1 p_6 &= -\mathcal{M}_1 q_6 + \mathrm{NL}_{p6}^{(2)} &&- \frac{\partial z/\partial T_1}{\bar{z}^2} p_1, \\ \mathcal{L}_1 q_6 &= \quad \mathcal{M}_1 p_6 + \mathrm{NL}_{q6}^{(2)} + f_c(t) p_6 &&- \frac{\partial z/\partial T_1}{\bar{z}^2} q_1.\end{aligned}$$

The nonlinear terms are $\mathrm{NL}_{p6}^{(2)}$ and $\mathrm{NL}_{q6}^{(2)}$ are:

$$\mathrm{NL}_{p6}^{(2)} = 2\mathrm{NL}_{p2}^{(2)} \qquad \text{and} \qquad \mathrm{NL}_{q6}^{(2)} = 2\mathrm{NL}_{q2}^{(2)}.$$

This can be reduced to a second-order non-constant coefficient inhomogeneous linear ODE for p_6:

$$\left(\mathcal{L}_1^2 + \mathcal{M}_1^2 + \mathcal{M}_1 f(t)\right) p_6 = \mathcal{L}_1 \mathrm{NL}_{p6}^{(2)} - \mathcal{M}_1 \mathrm{NL}_{q6}^{(2)} + \frac{\partial z/\partial T_1}{\bar{z}^2}\left(\mathcal{M}_1 q_1 - \mathcal{L}_1 p_1\right)$$

Since the operator on the LHS is the singular linear operator $\mathbf{L}$, we must apply a solvability condition:

$$\langle \tilde{p}_1, \mathbf{L} p_6 \rangle = 0 = \langle \tilde{p}_1, \mathcal{L}_1 \mathrm{NL}_{p6}^{(2)} - \mathcal{M}_1 \mathrm{NL}_{q6}^{(2)} \rangle - 2\frac{\partial z/\partial T_1}{\bar{z}^2} \langle \tilde{p}_1, \mathcal{L}_1 p_1 \rangle$$

since $\mathcal{M}_1 q_1 = -\mathcal{L}_1 p_1$. We define

$$\tau = \left\langle \tilde{p}_1, 2\left(\frac{dp_1}{dt} + \frac{\hat{\gamma}_1}{2} p_1\right)\right\rangle$$

as before and

$$\hat{\epsilon} = \left\langle \tilde{p}_1, \mathcal{L}_1 \mathrm{NL}^{(2)}_{p6} - \mathcal{M}_1 \mathrm{NL}^{(2)}_{q6}\right\rangle,$$

and obtain an equation for the slow (T_1) evolution of the amplitude z:

$$\tau \frac{\partial z}{\partial T_1} = \hat{\epsilon}\bar{z}^2.$$

Once the solvability condition has been imposed, the ODE can be solved for p_6 and q_6. The computed solution p_6 contains an arbitrary amount of p_1; the solution is made unique by specifying that $\langle \tilde{p}_1, p_6\rangle = 0$.

At third order in ϵ, the problem has the following structure:

$$\begin{aligned}
\mathcal{L}u_3 + \frac{\partial u_2}{\partial T_1} + \frac{\partial u_1}{\partial T_2} &= -\mathcal{M}v_3 + \mathrm{NL}^{(3h)}_u,\\
\mathcal{L}v_3 + \frac{\partial v_2}{\partial T_1} + \frac{\partial v_1}{\partial T_2} &= \quad \mathcal{M}u_3 + \mathrm{NL}^{(3h)}_v + f_c(t)u_3 + F_2 f_c(t) u_1.
\end{aligned}$$

We only need keep track of terms proportional to $e^{i\boldsymbol{k}_1\cdot\boldsymbol{x}}$ in our derivation of the bifurcation problem, so the $\partial u_2/\partial T_1$ and $\partial v_2/\partial T_1$ terms yield $p_6\partial\bar{z}^2/\partial T_1$ and $q_6\partial\bar{z}^2/\partial T_1$. The $e^{i\boldsymbol{k}_1\cdot\boldsymbol{x}}$ components of the nonlinear terms $\mathrm{NL}^{(3h)}_u$ and $\mathrm{NL}^{(3h)}_v$ are specified below.

Eliminating v_3, we obtain

$$\begin{aligned}
\left(\mathcal{L}^2 + \mathcal{M}^2 + \mathcal{M}f_c\right) u_3 = &-\mathcal{L}\left(\frac{\partial u_2}{\partial T_1} + \frac{\partial u_1}{\partial T_2} - \mathrm{NL}^{(3h)}_u\right)\\
&+ \mathcal{M}\left(\frac{\partial v_2}{\partial T_1} + \frac{\partial v_1}{\partial T_2} - F_2 f_c u_1 - \mathrm{NL}^{(3h)}_v\right).
\end{aligned}$$

The equation can only be solved for u_3 if a solvability condition is applied to the terms that are proportional to $e^{i\boldsymbol{k}_1\cdot\boldsymbol{x}}$, $e^{i\boldsymbol{k}_2\cdot\boldsymbol{x}}$ and $e^{i\boldsymbol{k}_3\cdot\boldsymbol{x}}$, and complex conjugates. If we take the inner product between $\tilde{p}_1$ and the $e^{i\boldsymbol{k}_1\cdot\boldsymbol{x}}$ component of the above, we find

$$\tau\frac{\partial z}{\partial T_2} = \sigma F_2 z + \left(\hat{A} + 2\hat{B}_{60}\right)|z|^2 z,$$

where τ and σ are unchanged from the rhombic calculations, and

$$\begin{aligned}
\hat{A} + 2\hat{B}_{60} = \Big\langle \tilde{p}_1, \Big(\frac{d}{dt} + \frac{\hat{\gamma}_1}{2}\Big)\mathrm{NL}^{(3h)}_u - \hat{\Omega}_1 \mathrm{NL}^{(3h)}_v\\
+ \left(-\mathcal{L}_1 p_6 + \mathcal{M}_1 q_6\right) 2\frac{\hat{\epsilon}}{\tau}\Big\rangle,
\end{aligned}$$

where we have used

$$\frac{\partial \bar{z}^2}{\partial T_1} = 2\bar{z}\frac{\partial \bar{z}}{\partial T_1} = 2\frac{\hat{\epsilon}}{\tau}|z|^2 z$$

and

$$\begin{aligned}
\mathrm{NL}_u^{(3h)} &= 2Q_{1r}(p_1p_2 + 3p_1p_3 + 2p_1\tilde{p}_5 + 2p_1p_6 - q_1q_2 - 3q_1q_3 - 2q_1\tilde{q}_5 - 2q_1q_6) \\
&\quad - 2Q_{1i}(p_1q_2 + 3p_1q_3 + 2p_1\tilde{q}_5 + 2p_1q_6 + q_1p_2 + 3q_1p_3 + 2q_1\tilde{p}_5 + 2q_1p_6) \\
&\quad + 2Q_{1r}(p_1p_2 + 3p_1p_3 + 2p_1\tilde{p}_5 + 2p_1p_6 + q_1q_2 + 3q_1q_3 + 2q_1\tilde{q}_5 + 2q_1q_6) \\
&\quad + 15C_r(p_1^2 + q_1^2)p_1 - 15C_i(p_1^2 + q_1^2)q_1, \\
\mathrm{NL}_v^{(3h)} &= 2Q_{1r}(p_1q_2 + 3p_1q_3 + 2p_1\tilde{q}_5 + 2p_1q_6 + q_1p_2 + 3q_1p_3 + 2q_1\tilde{p}_5 + 2q_1p_6) \\
&\quad + 2Q_{1i}(p_1p_2 + 3p_1p_3 + 2p_1\tilde{p}_5 + 2p_1p_6 - q_1q_2 - 3q_1q_3 - 2q_1\tilde{q}_5 - 2q_1q_6) \\
&\quad + 2Q_{2i}(p_1p_2 + 3p_1p_3 + 2p_1\tilde{p}_5 + 2p_1p_6 + q_1q_2 + 3q_1q_3 + 2q_1\tilde{q}_5 + 2q_1q_6) \\
&\quad + 15C_r(p_1^2 + q_1^2)q_1 + C_i(p_1^2 + q_1^2)p_1.
\end{aligned}$$

From the value of $\hat{A}$ calculated for rhombs, we can recover $\hat{B}_{60}$, which is effectively the cross-coupling coefficient for modes with wavevectors at 60°.

A.4. Reconstitution. At this stage, the pattern formation problem on a hexagonal lattice would take the form:

$$\begin{aligned}
\tau\frac{\partial z_1}{\partial T_1} &= \hat{\epsilon}\bar{z}_2\bar{z}_3, \\
\tau\frac{\partial z_1}{\partial T_2} &= \sigma F_2 z_1 + \left(\hat{A}|z_1|^2 + \hat{B}_{60}|z_2|^2 + \hat{B}_{60}|z_3|^2\right) z_1,
\end{aligned}$$

where z_1, z_2 and z_3 are amplitudes of $e^{i\boldsymbol{k}_1\cdot\boldsymbol{x}}$, $e^{i\boldsymbol{k}_2\cdot\boldsymbol{x}}$ and $e^{i\boldsymbol{k}_3\cdot\boldsymbol{x}}$. Similar equations are found for $\partial z_2/\partial T_1$ *etc.* Recall that the small factor ϵ has been used so that the amplitude of the original amplitude U is explicitly small: $U = \epsilon z_1(T_1, T_2)e^{i\boldsymbol{k}_1\cdot\boldsymbol{x}}p_1(t) + \ldots$

There is more than one way to combine these equations into a single ODE. Properly, we should consider only the case where the coefficient of the quadratic term $\hat{\epsilon}$ is itself small (order ϵ). This occurs either for small values of Q_1 and Q_2, or near a codimension-one line in (Q_1, Q_2) space:

$$\begin{aligned}
0 = \hat{\epsilon} &= \left\langle \tilde{p}_1, \mathcal{L}_1\mathrm{NL}_{p6}^{(2)} - \mathcal{M}_1\mathrm{NL}_{q6}^{(2)} \right\rangle \\
&= 2Q_{1r}\left\langle \tilde{p}_1, \mathcal{L}_1(p_1^2 - q_1^2) - \mathcal{M}_1(2p_1q_1) \right\rangle + 2Q_{1i}\left\langle \tilde{p}_1, \mathcal{L}_1(-2p_1q_1) - \mathcal{M}_1(p_1^2 - q_1^2) \right\rangle \\
&\qquad + 2Q_{2r}\left\langle \tilde{p}_1, \mathcal{L}_1(p_1^2 + q_1^2) \right\rangle + 2Q_{2i}\left\langle \tilde{p}_1, -\mathcal{M}_1(p_1^2 + q_1^2) \right\rangle.
\end{aligned}$$

Alternatively, we note that for many of these multi-frequency forced problems, $\hat{\epsilon}$ is small anyway [48, 49].

Having decided that $\hat{\epsilon}$ is small, we define a fast time scale t^*, related to the original time scale t by an order-one factor σ/τ:

$$\frac{d}{dt^*} = \epsilon\frac{\tau}{\sigma}\frac{\partial}{\partial T_1} + \epsilon^2\frac{\tau}{\sigma}\frac{\partial}{\partial T_2},$$

where ϵ is the original small parameter. We now scale the z's by $1/\epsilon$, so that the original amplitude U is implicitly small: $U = z_1(T_1, T_2)e^{i\boldsymbol{k}_1\cdot\boldsymbol{x}}p_1(t) + \ldots$, and obtain:

$$\frac{dz_1}{dt^*} = \lambda z_1 + \frac{\hat{\epsilon}}{\sigma}\bar{z}_2\bar{z}_3 + \frac{\hat{A}}{\sigma}\left(|z_1|^2 + B_{60}|z_2|^2 + B_{60}|z_3|^2\right) z_1,$$

where $\lambda = \epsilon^2 F_2$, so that the forcing amplitude is $(1+\lambda)$ times the critical amplitude, and $B_{60} = \hat{B}_{60}/\hat{A}$.

The advantage of reconstituting in this way is that the quadratic and cubic terms appear at the same order. The disadvantage is that the regime of validity ($\lambda \ll 1$, $\hat{\epsilon} \ll 1$, $z \ll 1$) is not made explicit. In particular, this validity condition will only be satisfied for hexagons when the coefficient of the quadratic term is small – which is precisely the limit required for the quadratic and cubic terms to be of the same order.

Finally, we scale the amplitudes once more by a factor of $\sqrt{|\sigma/\hat{A}|}$, rename the time variable back to t, and obtain:

$$\frac{dz_1}{dt} = \lambda z_1 + Q\bar{z}_2\bar{z}_3 + s\left(|z_1|^2 + B_{60}|z_2|^2 + B_{60}|z_3|^2\right) z_1,$$

with similar equations for z_2 and z_3, where

$$Q = \frac{\hat{\epsilon}}{\sigma}\sqrt{\left|\frac{\sigma}{\hat{A}}\right|} \qquad \text{and} \qquad s = \operatorname{sgn}\left(\frac{\hat{A}}{\sigma}\right)$$

(usually, $s = -1$).

Repeating the same reconstitution for the rhombic lattice results in

$$\begin{aligned}\frac{dz_1}{dt} &= \lambda z_1 + s\left(|z_1|^2 + B_\theta|z_2|^2\right) z_1\\ \frac{dz_2}{dt} &= \lambda z_2 + s\left(|z_2|^2 + B_\theta|z_1|^2\right) z_2\end{aligned}$$

where $B_\theta = (\hat{B}_{\text{indep}} + \hat{B}_{\text{res}}(\theta))/\hat{A}$.

The equations for other lattices can be found from combinations of the above, as can candidate equations for quasipatterns.